Eberhard Karls University Tübingen

Institute for Astronomy and Astrophysics

High Energy Astrophysics

Grazing Angle Proton Scattering on X-ray Mirrors – Measurements and Simulations

Thesis submitted for the degree of

Master of Science (M.Sc.) in Physics

by

Sarah Hanschke

Supervisor: Prof. Dott. Andrea Santangelo

Submitted: 20.12.2017

Erklärung

Ich versichere hiermit, dass ich die vorliegende Arbeit selbstständig verfasst und keine anderen als die im Literaturverzeichnis angegebenen Quellen benutzt habe.

Alle Stellen, die wörtlich oder sinngemäß aus veröffentlichten oder noch nicht veröffentlichten Quellen entnommen sind, sind als solche kenntlich gemacht.

Die Zeichnungen oder Abbildungen in dieser Arbeit sind von mir selbst erstellt worden oder mit einem entsprechenden Quellennachweis versehen.

Die Arbeit ist in gleicher oder ähnlicher Form noch bei keiner anderen Prüfungsbehörde eingereicht worden.

Tübingen, den 20.Dezember 2017

Sarah Hanschke

Contents

Abstract

Soft protons in the range of tens of keV up to a few MeV are focused much more efficiently by astronomical Wolter-type X-ray optics than estimated from simulations. In addition, they have a strong impact on the instrumentation of the telescopes: They contribute to the observational background and even degrade the performance of the instrumentation aboard the spacecraft.
The physical models describing soft proton scattering at grazing incidence angles, as it occurs for Wolter-type optics, are still matter of discussion and experimental data to validate the simulations are still rare.
In the last years an experimental setup has been established at the accelerator facility of the University of Tübingen in order to investigate grazing angle soft proton scattering on X-ray mirrors. Within this work, the setup has been extended with off-axis detectors, the analysis framework has been adjusted, new data has been obtained and evaluated, and new features in the experiment, e.g. passivated implanted planar silicon detectors have been studied via measurements and simulations.

Zusammenfassung

Niederenergetische Protonen im Bereich weniger keV bis zu ein paar MeV werden wesentlich effizienter durch astronomische Wolter-Röntgenoptiken fokussiert als es mit Simulationen vorhergesagt wurde. Diese Protonen haben großen Einfluss auf die Messinstrumente, die in den Teleskopen angebracht sind: Sie tragen zum Messuntergrund bei und verringern darüberhinaus die Performance der Messinstrumente an Bord des Raumfahrzeugs.
Die physikalischen Modelle zur Beschreibung von Streuprozesse an Wolteroptiken für niederenergetische Protonen unter streifenden Einfallswinkeln sind immer noch ein aktuelles Diskussionsthema und es gibt nur wenige experimentelle Daten, die zur Verifzierung von Simulationen eingesetzt werden könnten.
In den letzten Jahren wurde ein Experiment zur Erforschung der Streuung von niederenergetischen Protonen an Röntgenspiegeln unter streifenden Einfallswinkeln am Beschleunigerlabor der Universität Tübingen aufgebaut. Im Rahmen dieser Arbeit wurde der experimentelle Aufbau durch Off-Axis-Detektoren erweitert, die Datenanalyse an die Erweiterungen angepasst, neue Daten wurden gemessen und ausgewertet sowie neue Features wie beispielsweise Passivated Implanted Planar Silicon Detektoren durch Messungen und Simulationen untersucht.

1. Introduction

1.1. Soft Proton Effects on X-Ray Observatories

Protons in the low energy regime, so-called soft protons, can strongly influence astronomical X-ray measurements. They are within an energy range from around 10 keV up to 10 MeV. This range is limited at the low energy end by absorption in the dead layers at the entrance of the detectors and at high energies by the stopping of protons within the typical thickness of silicon detectors with thicknesses of a few hundred micrometers.

The effects of proton radiation on the performance of X-ray instruments can be subdivided into two types: Generating observational background and degradation of the instrumental performance.
Soft protons can contribute to the background of observations either via direct interactions in the sensitive detector volume or via interactions taking place in the surrounding material of the detector like creating secondary X-ray emissions, e.g. via fluorescence. Background studies using in-orbit data were performed for example for the European Photon Imaging Camera (EPIC) detectors of *XMM-Newton* [1] (cf. [2] on Background studies for *XMM-Newton*). The instrument collects soft protons that are accelerated by magnetospheric reconnection events in the vicinity of the sun and captured by the magnetosphere of the Earth. Times of high background are dominated by soft protons which emerge in flares with an intensity up to a factor 10 of the quiescent level of an astronomical measurement [3]. Soft protons are highly unpredictable and their spectra are very variable in shape and intensity (cf. [4]). Furthermore, the observation time of *XMM-Newton* is affected up to 40% by these particles [3].
More harmful on longer terms is the second type of soft proton effects – Soft protons

that are stopped in the sensitive region of solid state detectors and therefore deposit their complete energy in a small volume. The creation of lattice damage in the detector bulk leads to increased leakage currents and, therefore, to a degradation of the energy resolution as well as to a reduction of charge collection efficiency (charge transfer efficiency (CTE)) in CCDs.

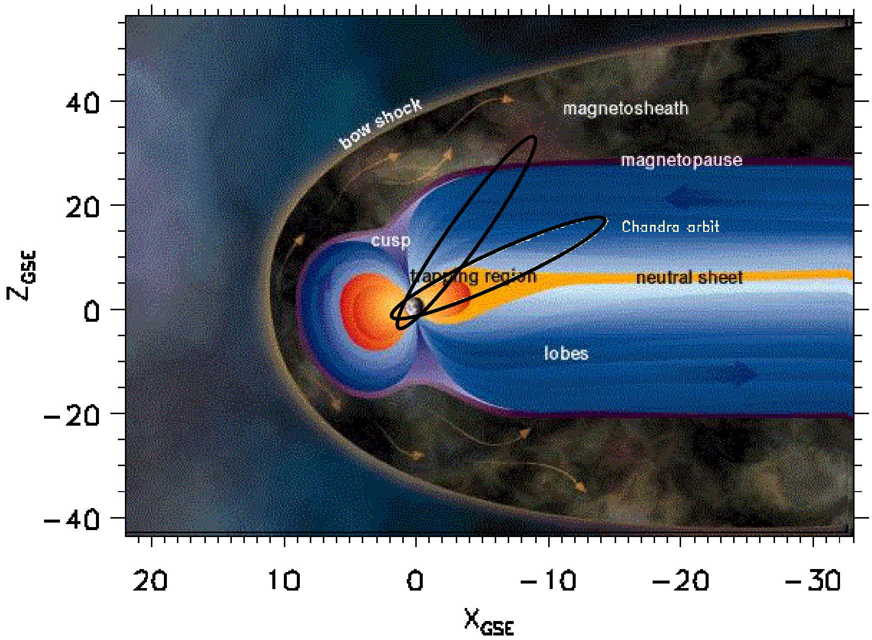

Figure 1 The orbit of the *Chandra X-ray observatory* in geospace is similar to the orbit of *XMM-Newton*. When *Chandra* was launched there have been no detailed models of the radiation environment of the spacecraft's orbit – in particular no models of low energetic protons in the outer magnetosphere, magnetosheath, and solar wind regions (see [5]).

A well-studied example for this type of soft proton effect is the degradation of the front-illuminated CCDs of *Chandra's* [6] Advanced CCD Imaging Spectrometer (ACIS) instrument. The ACIS instrument hosts ten CCDs: eight front-illuminated CCDs where a decrease in the charge transfer efficiency was noticed already shortly after the launch of the observatory and two of them are back-illuminated which remained unharmed. As main source of the damage, Kolodziejczak et al. [7]

found soft protons that are scattered off the mirrors of the observatory (see [8]). Operating procedures have been modified so that ACIS won't remain in the focal position when the X-ray observatory passes radiation belts (cf. [9]).

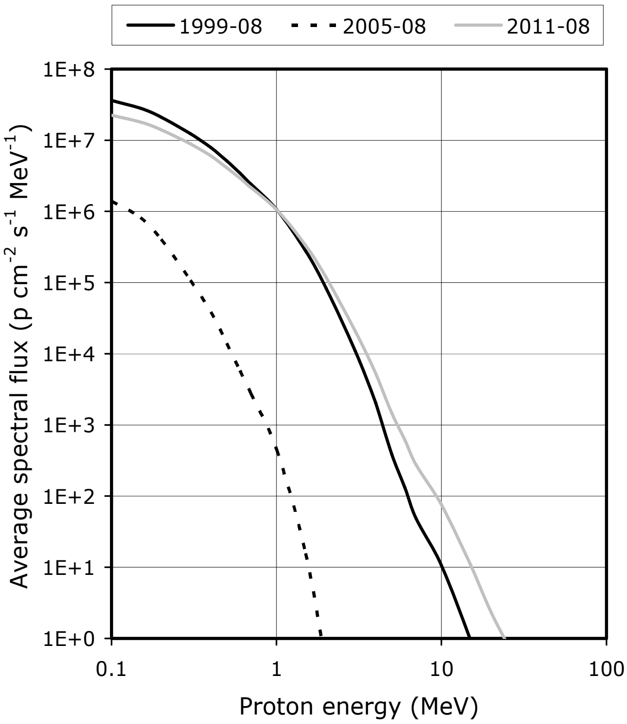

Figure 2 The orbit-averaged trapped-proton spectrum shows that the proton flux intensity on the spacecraft varies with the evolution of *Chandra's* orbit. The proton spectra are plotted with a black line for the first exposure to trapped protons (1999), with a black dashed line (2005) and a grey line another six years later (2011). The data have been found by using the SPace ENvironment Information System (SPENVIS)[1] to calculate the flux environment of *Chandra's* orbit with the standard AP8 radiation environment by NASA (see [10]).

At the time, when *Chandra* was launched, there have been no models of the flux environment as for example shown in Fig. 2 of the spacecraft's orbit (see Fig. 1). Especially for protons in the region of 100 keV up to about 200 keV where the flux has its maximum (see Fig. 2) the capability of the mirrors to focus soft protons has been underestimated.

1.2. Grazing Incidence Proton Scattering

1.2.1. Current State of Research

Following Fioretti [11] and Spiga et al. [4], three models have been proposed to describe the proton scattering off of astronomical X-ray mirrors: The multiple Rutherford scattering model, Remizovich's theory as an extension of the theoretical descriptions after Firsov and a totally different scattering mechanism proposed by Aschenbach.

a) Multiple Rutherford scattering: Protons interact with the electric field of nuclei of the X-ray mirror coating, e.g. gold and are scattered. Multiple scatterings of the protons may enhance the deflection angle. The final energy and angular distribution depends on the number of subsequent scatterings, the incident proton energy and the incidence angle (see [11] and [4]). The multiple Rutherford scattering model has been used for simulations with the TRIM[2] software (cf. [7]) and GEANT4 ([13]) for *Chandra* and *XMM-Newton* [11].

b) Aschenbach [14] is a critic of the multiple scattering description. He proposed a model, in which protons are treated as de Broglie waves. In combination with an refraction index less than one the model predicts a total external reflection of protons. The reflection mechanism according to Aschenbach is very efficient without energy losses or angular dispersion. The angular spread which was ascertained in reflectivity experiments is attributed to the roughness of the mirror surface analogue to the photon scattering process of X-rays [4].

[2] TRIM (Transport and Range of Ions in Matter) is part of the SRIM (The Stopping and Range of Ions in Matter) software package: www.srim.org. (see also [12]).

c) Firsov's and Remizovich's model: Dichter and Woolf [15] as well as Lei et al. [16] found that the multiple scattering description is unable to explain proton scattering for small incidence angles. So far, the models that have been implemented, e.g. in GEANT4 could not reproduce the grazing angle incidence scattering of protons. Experimental studies, e.g. the ones of Winter, Wilke and Bergomaz [17], Pfandzelter and Stölzle [18] and the simulations of Song and Wang [19], demonstrated that protons incident on a surface interact with the material even before they encounter the first layer of atoms – Protons incident on a solid surface at grazing angles do not interact with the surface material atoms via a multiple scattering process. Instead, they are reflected off the surface in the electron plasma cloud outside the material [16].

A scattering behavior described by Firsov's theoretical scattering distribution [20] is seen as a more suitable model instead (see 1.2.2 for further details on the theory). The angular distribution is more peaked after Firsov's process than it is for the multiple scattering (see [4]). It was implemented in GEANT4 by Lei et al. [16] and also proposed by Dichter and Woolf [15]. The proton funneling efficiency is increased in the Firsov process which means that the beam is much more collimated. Following the results of Lei et al. [16] about five times more protons strike the focal plane in a GEANT4 simulation than without the Firsov process [11].
The scattering model of Remizovich [21] gives a two-dimensional and, therefore, more precise distribution for particles reflected by solids at grazing angles (see Section 1.2.3). Remizovich holds also a scattering description for the distribution in azimuthal direction, whereas the azimuthal scattering distribution is already integrated in the model of Firsov. Currently Remizovich's model is implemented in GEANT 4 (see, e.g. [8]) but experimental data to validate the simulations are

still rare. An older example where Remizovich's model was already tested with experimental data is the publication of Kuwata et al.[22]. They could show a good agreement of experimental and theoretical values for small scattering angles when the Remizovich curve was normalized to the maximum of the particle yield of the experimental data.

The models of Firsov and Remizovich are introduced briefly in the following section as well as the connection between the models. Whereas Firsov's theory was used to compare with experimental data in prior measurements (cf. [23]) and implemented as a physics process in GEANT4 (cf. [16]) Remizovich's model is used more frequently in recent times to compare theory with simulations (cf. [8]) or experimental results (see the last chapter of this work, Section 4.3).

1.2.2. Firsov's Scattering Description

Firsov developed an analytical description for protons that are scattered on a mirror-like surface based on the surface plasmon model. The scattering process is seen as purely elastic and furthermore energy loss is not taken into account [23, 24].[3] In Firsov's probability distribution an integration over the azimuthal angles is already performed. The distribution given in Eq. 1 is adjusted to the coordinate system of the scattering measurements at the accelerator facility in Tübingen (see [24] for the coordinate transformation formula) and represents the behavior of particles in elastic collisions with a dense medium and at glancing angles (cf. [8]).

$$F(\Theta) = \frac{3}{2\pi\Psi_0} \cdot \left(\frac{\Psi_0(\Theta - \Psi_0))^{\frac{3}{2}})}{\Psi_0^3 + (\Theta - \Psi_0)^3)} \right) \tag{1}$$

[3] Firsov's publication is only available in Russian language (see [20]). Therefore, (secondary) sources in English have been chosen to obtain further information about Firsov's theory.

$F(\Theta)$ describes the probability for a particle with incidence angle Ψ_0 to scatter at an angle Θ. The function peaks for small values of Ψ_0.

1.2.3. Remizovich's Scattering Description

Remizovich gives a two-dimensional model including an azimuthal and vertical scattering distribution for particles scattered off of solids at grazing angles. To obtain the distribution Remizovich solves the Boltzmann transport equation via the diffuse approximation and the continuous-slowing-down approximation[4]. The elastic model of Remizovich does not depend on the reflecting material in its mathematical form (see [8]).

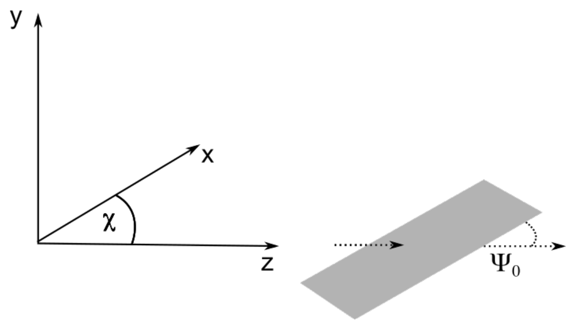

Figure 3 Remizovich's angle convention, where Ψ_0 is the incidence angle in relation to the target and χ is the azimuth angle.

The angle convention used by Remizovich is sketched in Fig.3, where Ψ_0 is incidence angle and χ is the azimuth angle. Remizovich's solution[21] of the transport

[4]A brief explanation of the continuous-slowing-down approximation (CSDA) can be found on the Appendix of the website of the PSTAR program (stopping-power and range tables for protons) of the National Institute of Standards and Technology (NIST) [25].

equation in the elastic case is given via

$$W_{\mathrm{el}}(\chi.\psi) = \frac{1}{12\pi^2\sqrt{\psi}} \cdot \left[\frac{\omega^4}{1+\omega^2} + \arctan(\omega)\right] \tag{2}$$

with the substitution

$$\omega = \sqrt{\frac{3\psi}{\psi^2+\psi+1+(\frac{\chi}{2})^2}}. \tag{3}$$

The function is normalized to

$$\int_{-\infty}^{\infty} \mathrm{d}\chi \int_0^{\infty} W_{\mathrm{el}}(\chi,\psi)\mathrm{d}\psi = 1.$$

The distribution after Remizovich has been transformed into the experimental frame of the scattering experiment at the accelerator facility in Tübingen. After a coordinate transformation into the laboratory system of the experimental setup (following Guzmán et al.[24])

$$\begin{pmatrix} \psi_0 \\ \theta - \psi_0 \\ \chi \end{pmatrix}_{\text{Tübingen}} \rightleftharpoons \begin{pmatrix} \zeta_0 \\ \zeta \\ \varphi \end{pmatrix}_{\text{Remizovich}} \tag{4}$$

the distribution after Remizovich is:

$$\mathrm{R}(\chi,\theta) = \frac{1}{12\pi^2\psi_0\sqrt{\psi_0(\theta-\psi_0)}} \cdot \left[\frac{\omega^4}{1+\omega^2} + \arctan(\omega)\right] \tag{5}$$

with the substitution

$$\omega = \sqrt{\frac{3(\theta-\psi_0)\psi_0}{(\theta-\psi_0)^2+(\theta-\psi_0)\psi_0+\psi_0^2+(\frac{\chi}{2})^2}}. \tag{6}$$

As for the original, it is normalized to one:

$$\int_{-\psi_0}^{\infty} \mathrm{d}\chi \int_{0}^{\infty} \mathrm{R}(\theta, \chi)\mathrm{d}\theta = 1.$$

Eq. 5 has been used to compare Remizovich's model to the experimental results of measurements with on- and off-axis detectors shown and discussed in Section 1.2.3.

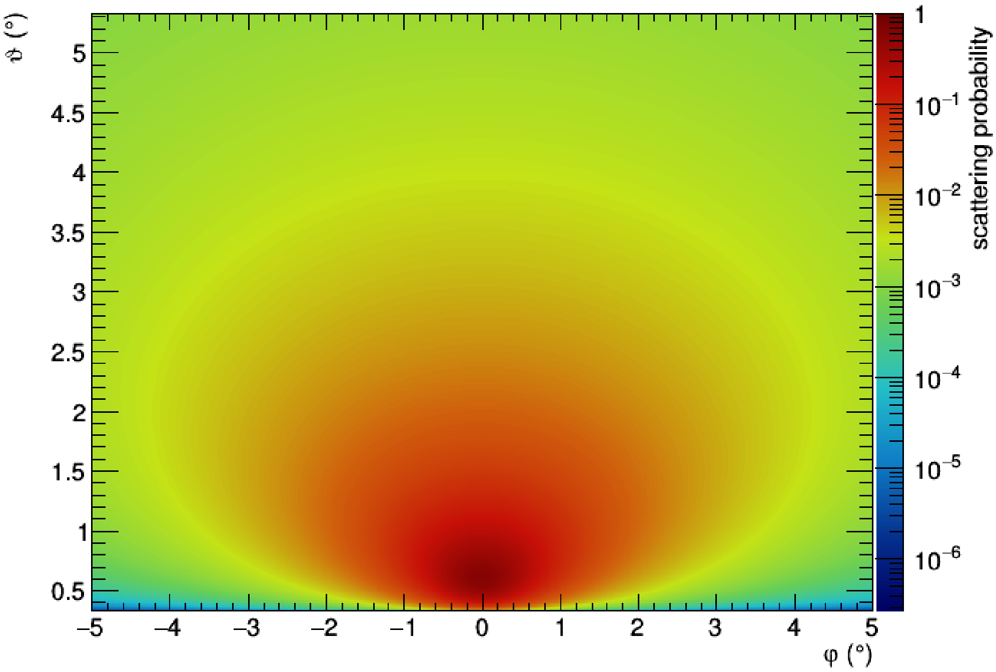

Figure 4 Two-dimensional scattering probability distribution after Remizovich for the azimuth angle $\chi = 0.33°$ (Eq. 5).

Fig. 4 presents the distribution of Eq. 5 in a two-dimensional and color-coded plot. Since the formula is normalized to one, the integral over the distribution is one which means an idealization was made, that 100% of the incoming particles are scattered (there are no secondaries, no backscattered particles considered etc.).

1.3. Aim of this Thesis

This work contributes to the grazing angle proton scattering experiments conducted at the accelerator facility in Tübingen: Studies have been made via simulations and experimental tests to improve the experimental setup and furthermore, new measurement data have been gathered and analyzed with the improved setup.

The following improvements were conducted: the setup has been extended with off-axis detectors (see Section 3.2) to gain insights on the azimuthal scattering distribution of soft protons. Passivated implanted planar silicon (PIPS) detectors have been installed and studied (see Section 3.3) to be able to measure at lower proton energies and the software for the evaluation has been adjusted to the alterations (see Section 2.5). The energy calibration procedure for the measurements has been refined (see Section 2.4) and a more efficient energy calibration method has been evaluated (see Section 3.4). And finally, new off-axis data have been analyzed and compared to the theoretical model of Remizovich (see Section 4).

The further layout of this thesis is as follows: Chapter 2 introduces the experimental setup at the accelerator facility in Tübingen, the detector types that have been used for the measurements, the calibration procedures and the analysis framework for the evaluation of measurement data.
Studies to evaluate improvements are presented in Chapter 3 and results of data obtained with the upgraded experimental setup are shown in Chapter 4.

2. Experimental Setup

2.1. Accelerator Facility

An experimental setup to measure grazing angle soft proton scattering has been established at the accelerator facility of the University of Tübingen in the last few years (cf. [26]). The main components of the facility – the accelerator and beam lines – are shown in Fig. 5.

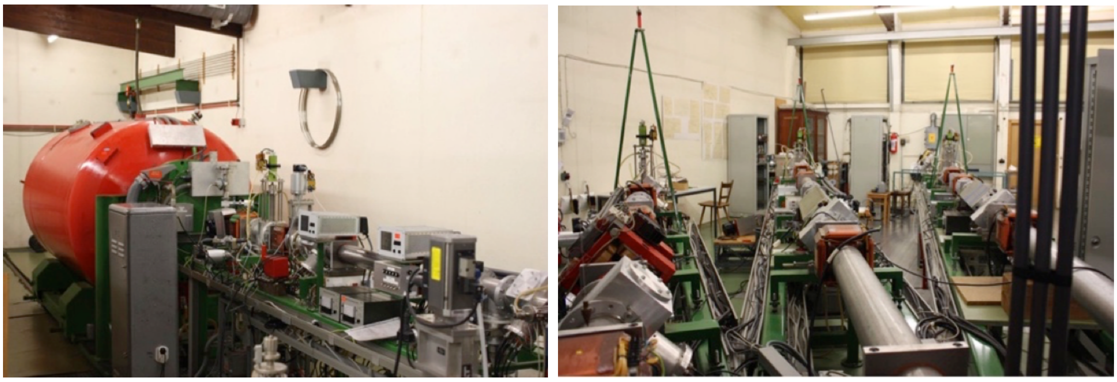

Figure 5 Accelerator and beam lines at the accelerator facility in Tübingen. The 3 MV Van de Graaff accelerator is located in a red tank at the beginning of the beam line (left) and the beam lines 1 to 3 (left to right on the right). Backscattering calibration measurements are conducted with a D-shaped chamber at beam line 2 and the grazing angle scattering experiment is located at beam line 3 (Credit: S. Diebold).

The machine is a 3 MV single-ended Van de Graaff accelerator (HVEC KN-300) capable of producing light ion beams in the energy range of about 500 keV up to 2.5 MeV and beam currents between 200 nA and 40 µA can be adjusted. A generating voltmeter (GVM) measures the terminal voltage and thereby the beam energy can be determined [27]. To calibrate the GVM, the gamma rate of the reaction ^{27}Al(p,γ)^{28}Si is measured: with a NaI(TI) (Thallium activated Sodium iodide) scintillation detector a sharp resonance can be determined at 992 keV [28].

Gases like hydrogen, deuterium, helium or ^{13}C-enriched CO_2 are accessible as ion sources for the beam [26].Therefore, the accelerator can produce several other light ion types besides protons, for example deuterons, alpha particles, carbon, oxygen and helium ions which are also planned for future scattering measurements, since helium is the second most abundant particle in orbital radiation. Altogether, the mentioned ions cover the most abundant ion constituents of orbital radiation [29]. These ions are provided by a radio frequency plasma source located in the high-voltage terminal, which ionizes the source gas to the charge state 1+ [26]. The beam is bent by 95° with an analyzing magnet which helps selecting the ions via momentum separation and also stabilizes the terminal voltage on a 10^{-3} level via feedback to the voltage regulation system [23].
The facility in Tübingen features six beam lines and the scattering setup is mounted on beam line 3 (see Fig. 5). Beam lines are selected via a switching magnet. Dipole magnets along the beam line are used to direct the beam through the beam tubes. And two pairs of double quadrupole magnets are installed to focus the beam.

2.2. Experimental Setup

The experimental assembly in the accelerator hall as well as an interior view on the setup via a crossectional CAD graphic can be seen in Fig. 6.
In Fig. 7 a schematic of the experimental setup is shown where Ψ is the incidence angle and Θ the scattering angle. Θ is measured in relation to the incoming beam. The beam enters the experimental setup from the left-hand side through a pair of slits (consisting of four adjustable copper parts) with a rectangular aperture to check the alignment with the setup. It passes a pinhole aperture with a circular opening and a diameter of 100 μm which reduces the beam current and therefore the rates on the monitor detectors.

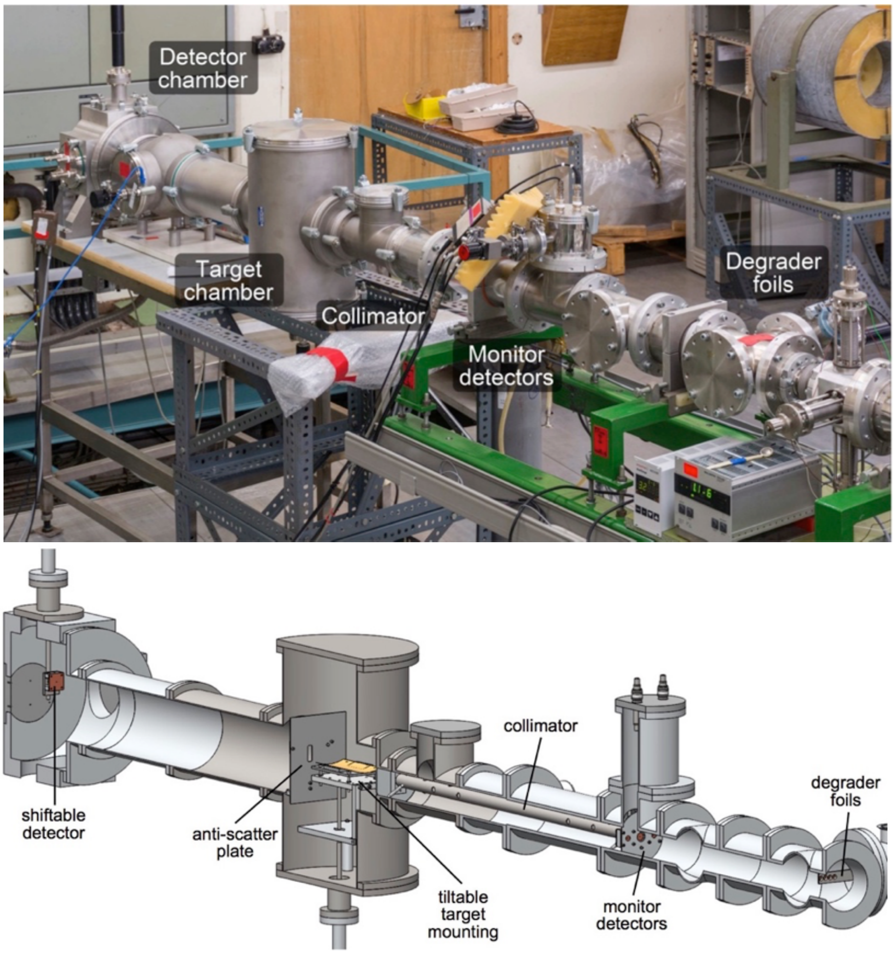

Figure 6 View of the experimental setup at the accelerator facility in Tübingen (top) and a crossectional CAD graphic (bottom) (Credit: [23]). In both pictures, the beam enters from the right hand side. The degrader foil widens the beam and provides flux to the monitor detectors on the left and right to the collimator entrance. Its material can be changed via a movable holder where different materials with different thicknesses are mounted. Behind the collimator, the protons are scattered at the target in the target chamber. The particles are measured with a shiftable detector (or a shiftable detector array) at the end of the beamline.

A degrader foil widens the beam providing constant flux on the monitor detectors peripheral to the beam which is crucial for the proper normalization of the measured scattering rates to account for fluctuations of the incoming beam. These fluctuations originate from changes of the terminal voltage, variations in the ion production in the source and also from drifts of the magnetic fields of the bending magnets. The degrader foil is a few micrometers thick and consists of a metal material, e.g. copper or aluminum. The material is selectable via a movable mounting bracket.

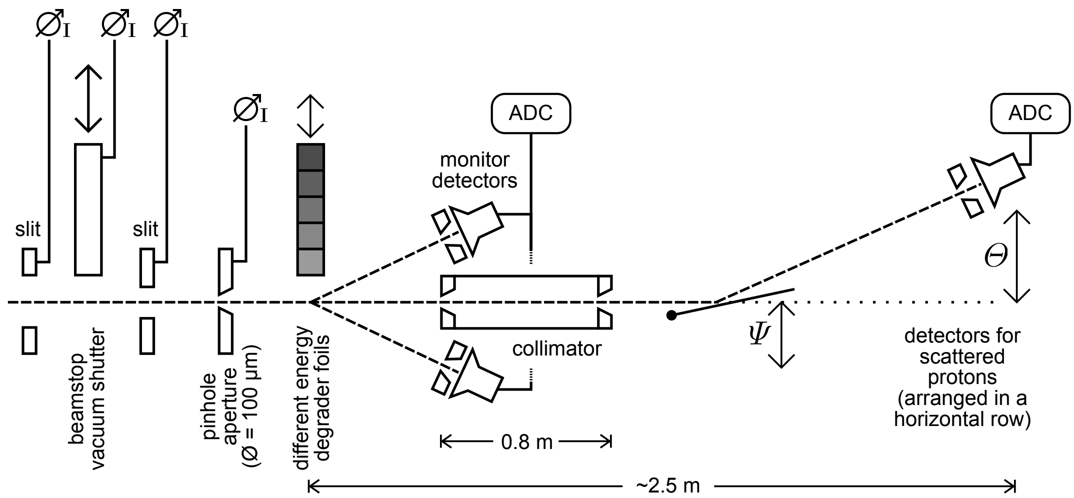

Figure 7 Schematic of the experimental setup (Credit: [29]). The beam enters from the left and passes two pairs of slits that align the beam. The beam is widened by a degrader foil and therefore the two peripheral monitor detectors are provided with constant flux which is important for the normalization of detected scattered particles. After the collimator, the pencil beam hits a target under an incidence angle Ψ and scattered protons (scattering angle Θ) are measured with detectors at the end of the beamline.

A collimator with 78 cm length as well as aperture diameters of 1.0 mm at the entrance and 0.3 mm at the exit directs the 300 µm pencil beam to a target on a

120 mm long tiltable table. A part of an *eROSITA* (extended Roentgen Survey with an Imaging Telescope Array) [30] mirror shell with 6 cm width and 12 cm length was used as scattering target. It consists of a 270 µm nickel substrate with a 50 nm gold coating.

Via the collimator apertures, the maximum opening angle is restricted to 0.1° (1.7 mrad) to regulate the transmitted flux and to preserve angular precision. The height of the target table is changed via setscrews, so that it can be adjusted to various target geometries and thicknesses. The incidence angle Ψ is changed via a linear manipulator from beneath with a precision of 0.01 mm (corresponding to an angular precision of 0.006° (0.1 mrad)). At the end of the target chamber, an aluminum anti-scatter plate with 3 cm height and 1 cm width is mounted. The plate reduces the flux which is produced by protons that have been scattered at the inside of the beam line, i.e. the proton background of the measurements.
The scattered protons that pass the anti-scatter plate are measured with a vertically shiftable detector (or up to four detectors mounted in a detector array, depending on the measurement) at a distance of 933 mm to the center of the target table. The detector mounted in the horizontal center of the beam direction is called on-axis as the detectors left and right to the horizontal center are called off-axis detectors. The detectors are also shiftable in the vertical direction with a linear manipulator similar to the one used for the tilting of the target table. From the beam line center, the detectors can be moved upwards to a maximum of 75 mm which equals a maximal scattering angle Θ of about 4.5° (80 mrad). Detector apertures and the detectors solid angles Ω vary depending on their mounting position in the array. The on-axis detector has an opening diameter of 1.25 mm corresponding to a solid angle of 1.4 µsr, off axis detectors on the left and right have aperture sizes of 1.5 mm and an additional off axis detector on the very right has an aperture size of 2 mm. The detectors are mounted at a distance of 32 mm to

the on-axis detector, i.e. in case of the very right detector at a distance of 64 mm to the central detector.
All detectors in the array are read out with a fourfold peak-sensing ADC (analog-to-digital converter). Additionally, the fourth ADC channel carries a pulser signal which is split and as well fed into a scaler to account for dead time. To gather information about the conversion efficiency of the ADC channels, the ratio between pulses incoming to the ADC and the scaler value is determined (cf. [23]).

2.3. Solid State Detectors: Silicon Surface Barrier and Passivated Implanted Planar Silicon Detectors

The detectors used in the experimental setup are solid state detectors like silicon surface barrier (SSB) detectors or passivated implanted planar silicon (PIPS) detectors. These detectors are made of semiconductor materials: They operate based on a small energy gap between the semiconductor valence and conduction bands. With a small energy deposition, electrons can be moved from the valence to the conduction band and therefore, holes are created in the valence-band. By applying an electric field, the two charge carriers – electron and hole – drift towards electrodes and produce a signal [31]. A common material for solid state detectors is silicon as used, e.g. for SSB and PIPS detectors.

An SSB detector has an evaporated gold (or aluminum) surface whereas a PIPS detector has a passivated, ion implanted surface as an entrance window. This makes the face contact of the PIPS detector much more rugged and as opposed to the SSB detector it can be handled and cleaned (and heat sterilized). The SSB detector has an extremely sensitive metallic window, e.g. gold or aluminum. Touching this window or trying to remove any contaminations damage the window and lead to performance degradations of the detector [32]. As shown in Fig. 8 the

silicon wafer of the SSB detector is epoxied at its junction edges. The PIPS detectors have their junction edges within the silicon wafer [33]. In the manufacturing process of PIPS detectors, ion implantation and photolithographic techniques are combined [34]. Therefore, PIPS detectors have much smaller leakage currents than SSBs, and their noise levels are smaller than the ones of SSB detectors [35] resulting in an improved energy resolution around 6-12 keV [36] due to a thinner entrance window (<50 nm) than an SSB detector (∼80 nm) [36] and and the noise reaches up to 50-60 keV (see studies in section 3.3).
The SSB detectors used in the experiment have an 8 mm sensitive diameter, an energy resolution between 10-20 keV and typically count rates up to $2{\cdot}10^5\,s^{-1}$ can be achieved without pile-up. Their low energy threshold lies in between 80-100 keV.

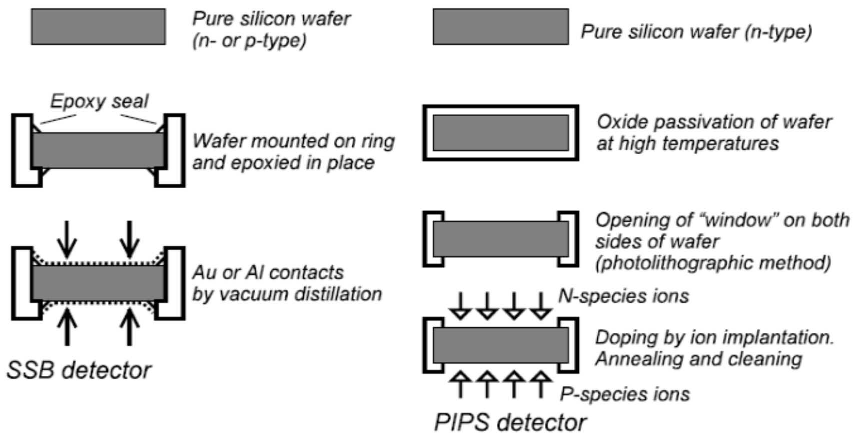

Figure 8 Simplified comparison of the manufacturing of an SSB detector (left) and a PIPS detector (right) (Credit: [32]). The silicon wafer of an SSB detector is epoxied on a ring and has a very thin metallic contact, e.g. gold or aluminum on the front.
The PIPS detector is "passivated" via an oxide layer created at high temperatures. The oxide is then removed via photolitographic methods in the area where the entrance window of the detector will be. A thin layer of silicon is implanted with ions by using an accelerator. Through annealing, the radiation damage in the implanted layer is cleared [34].

2.4. Calibration Procedures

Three calibration procedures are applied for the grazing angle scattering measurements:

a) an angular calibration to calibrate the range of incidence angles for the setup

b) a detector energy calibration via Rutherford backscattering with three different targets to determine the ADC channel-to-energy mapping

c) a flux calibration to normalize the flux on the monitor detectors and on the target.

In preparation for the measurements the incidence angles need to be calibrated. Furthermore, the detectors used for the measurements are calibrated before conducting measurements. The flux calibration is done every time after a measurement before the accelerator is turned off between the next measurement, whereas the angular and detector energy calibration are only performed for each measurement setup.

a) Angular Calibration

The position of the target, i.e. the incidence angle Ψ as well as the position of the detectors, i.e. the scattering angle Θ are selectable via linear manipulators (see Section 2.2). The manipulator positions then have to be converted into angles: If the manipulator position related to $\Theta = 0\,^{\circ}$ is known the scattering angle can be determined from the geometry. The incidence angle needs to be calibrated and the limits of the range of incidence angles need to be determined as the incident flux only hits the mirror entirely within a certain range of incidence angles. This range depends on the height of the target table.

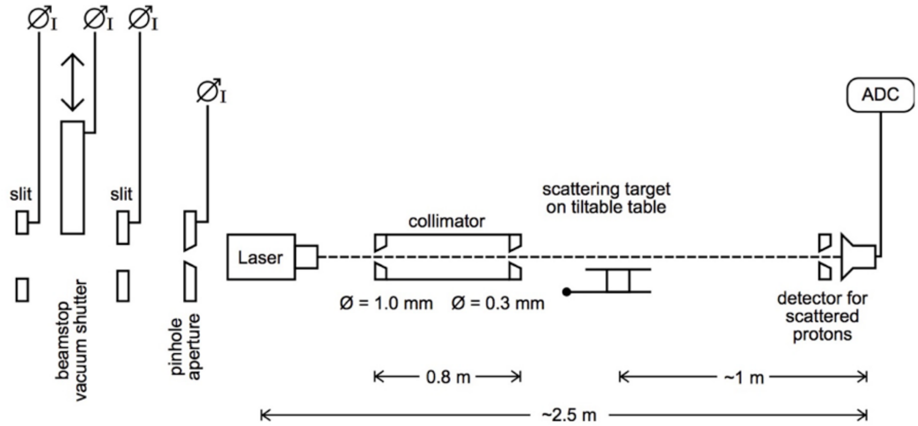

Figure 9 Schematic diagram of the angular calibration procedure: A laser is put in front of the collimator entrance pointing in the direction of the proton beam (here: from the left to the right), i.e. the silicon surface barrier detectors. For the angular calibration, the scattering target is tilted successively into the laser beam and measured with the detector at the end at which position the target covers the laser beam completely. This is the position of the minimum incidence angle (Credit: S. Diebold).

For the calibration of the incidence angles a 445 nm solid-state laser is used as the X-ray mirror targets reflect visible light and it is also detectable with an SSB. The laser is put into the beamline after the pinhole aperture and adjusted until the intensity is at its maximum at the exit of the collimator (see Fig. 9). First, the $\Theta = 0\,^\circ$ position of the detectors needs to be measured then the mirror will be shifted in the course of the beam. Through the condition for specular reflection $\Psi = \frac{\Theta}{2}$ the angles which correspond to the different manipulator positions are determined.

The minimal incidence angle is at the position where the target blocks the primary laser beam completely. The tilt angle of the mirror is increased step by step and at each position the reflected beam is measured with the detector (cf. [23]).

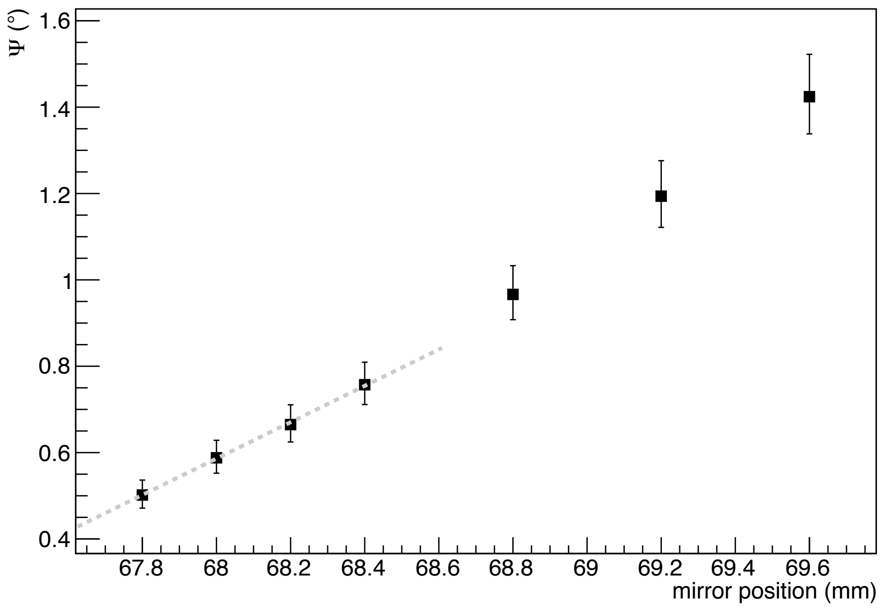

Figure 10 Example for a laser calibration plot with mirror positions and corresponding mirror angles Ψ. The data are taken with an *eROSITA* mirror sample. The grey dotted line is a partial linear fit including the smaller angles in the range of interest.

Fig. 10 shows an example for the laser calibration data taken with an *eROSITA* mirror sample. The plot is partially linear fitted to the smaller values which are within the range of interest. For the larger incidence angles and mirror positions a linear fit would also apply but with increased slope. The change of slope is still a matter of discussion and yet an unanswered question. Therefore, for the measurements only the explicit mirror positions and corresponding laser calibrated incidence angles obtained from the calibration graph are used. An example plot (Fig. 10) and the mirror and detector positions with associated incidence angles are shown in Table 1.

Table 1 Mirror and detector position values and incidence angle values corresponding to the laser calibration example shown in Fig. 10.

mirror position (mm)	detector position (mm)	mirror angle Ψ (°)
67.80	16.30	0.50
68.00	19.10	0.59
68.20	21.60	0.66
68.40	24.60	0.76
68.80	31.40	0.97
69.20	38.80	1.19
69.60	46.30	1.42

b) Detector Energy Calibration

The SSB detectors have been energy calibrated via backscattered protons off of known targets. Three targets have been used to calibrate the SSBs used in current measurements: carbon (^{12}C), gold (Au) and aluminum (Al). Detectors and targets have been mounted in the D-chamber at the end of beam line 2 (see Fig. 11). Electronic components and cables used for the scattering measurements remain the same for the backscattering measurement.

For the calibration, the ADC channel-to-energy mapping is determined via the positions of the high-energy edges of the spectra. For this purpose, different fits are applied to the spectra depending on the backscattering target material. The fit routines for this calibration procedure have been improved, so that there is a triple Gaussian fit for thin targets (a carbon (^{12}C) target) and a box-like fit combined with a linear offset for the thick targets (gold and aluminum).

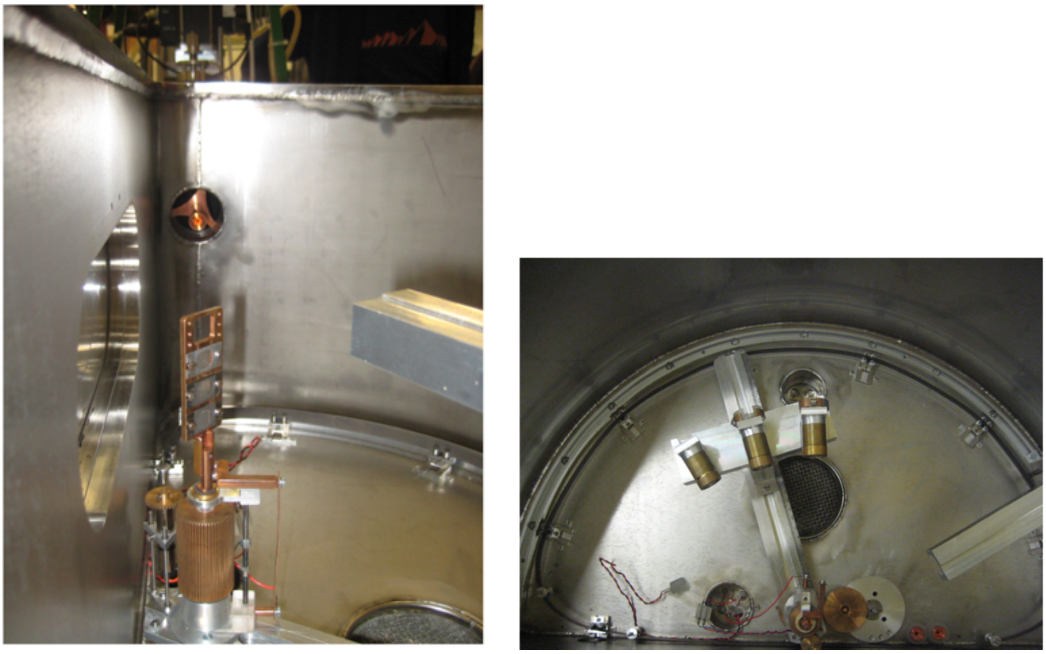

Figure 11 Insight in the D-chamber where the detector calibration is performed at the end of beam line 2. The three targets are mounted in a vertical row on an angle adjustable holder (left). In the background slightly above the target holder the beam enters the D-chamber in the direction of the targets. On the right the chamber is shown from above to present the mounting of the three detectors in backscattering positions. The detectors are movable to measure different backscattering angles. From this perspective, the beam enters the D-chamber from the right.

As fit function for the box-like fit

$$f(x) = \mathrm{a}x + \mathrm{b} + \begin{cases} \text{constant} + \text{slope} \cdot (x - x_{\text{edge}}) & : x \leq x_{\text{edge}} \\ e^{\frac{(x-x_{\text{edge}})^2}{2\sigma^2}} & : x > x_{\text{edge}} \end{cases} \tag{7}$$

is implemented in the calibration procedure where a and b are parameters of a common linear offset, x_{edge} is the transition edge of the function, and constant and slope describe the linear part below the transition edge. The shape of the transition is described by a Gaussian function (see Eq. 7). An example for these fit procedures can be seen in Fig. 12.

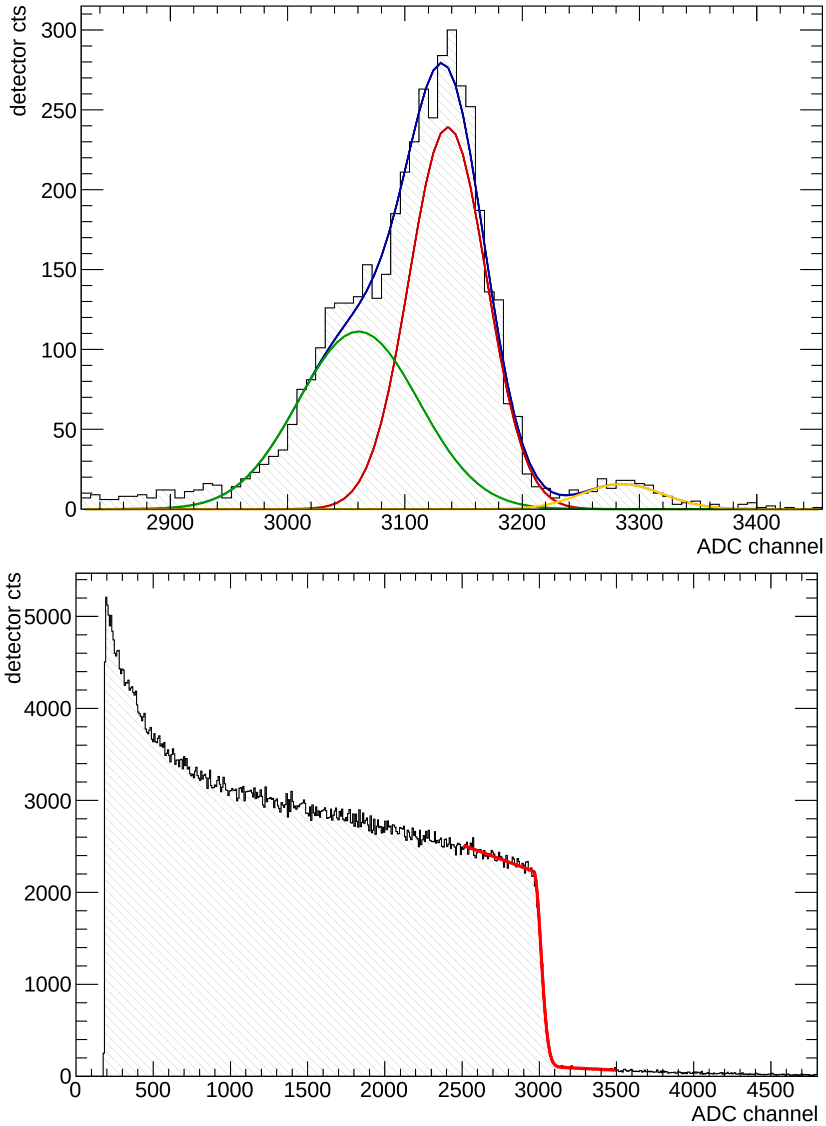

Figure 12 Example for a calibration plot of a thin ^{12}C target with a triple Gaussian fit for 995 keV protons and a detector at a 135° backscattering position (top). The blue fit curve is the resulting fit from the three peaks in the spectrum. The peak on the very left originates from ^{12}C, the second peak from the heavier ^{13}C and the small peak on the right belongs to ^{16}O. The second plot (bottom) shows an example for a thick gold target with a box-like fit for the edges for a 730 keV proton beam and a detector also at a 135° backscattering position.

The high-energy edges of the fits then are plotted in a graph and a linear fit is applied.

Table 2 High-energy edge values of 135 ° backscattered protons from three target materials for a 995 keV proton beam corresponding to Fig. 13.

Target material	Proton energy (keV)
^{12}C	746.5
Al	875.9
Au	977.8

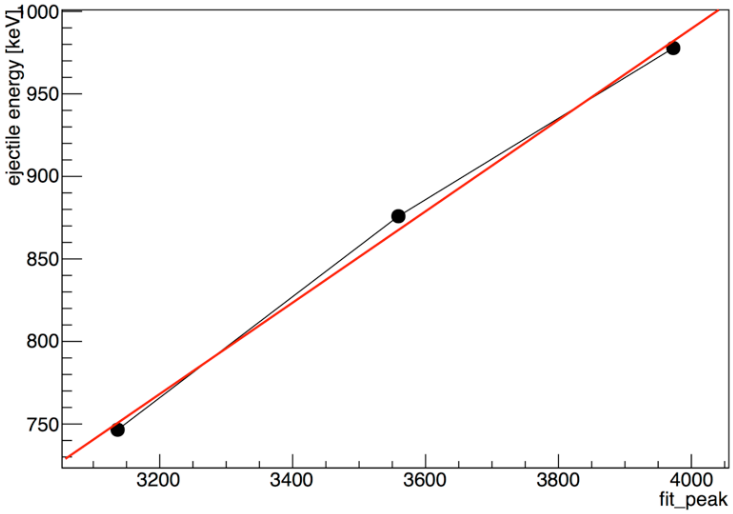

Figure 13 ADC channel-to-energy mapping with the high-energy edges of the measured spectra in case of a 995 keV proton beam and for the detector mounted at a 135° backscattering position. The three high-energy edges (fit peaks) corresponding to the three calibration targets used are plotted on the x-axis against the ejectile energy on the y-axis. The first fit peak (from the left to the right) belongs to the thin carbon target, the second one is the thick aluminum target and the third one belongs to the gold spectrum. The parameters of the linear fit (red line) are used to calibrate the spectra of the grazing angle scattering measurements.

An example graph is shown in Fig. 13 and the corresponding high-energy edges are summarized in Tab. 2). The parameters from the fit are used for the ADC channel-to-energy mapping.

c) Flux Calibration

For each beam energy that is used for the measurements the target will be tilted out of the beam and a detector will be put in front of the collimator exit to measure the incident flux at the primary beam position (see Fig. 14) as the proton beam varies not only in direction but also in flux. The flux calibration is needed to normalize the measured flux on the two monitor detectors and relate it to the incident flux on the target. Moreover, the degrader foils widen the beam energy-dependent which is why the calibration needs to be done for every energy used for the measurements. An uncertainty of ±10% for the incident flux on the target has been estimated for employing this calibration method (see [23]).

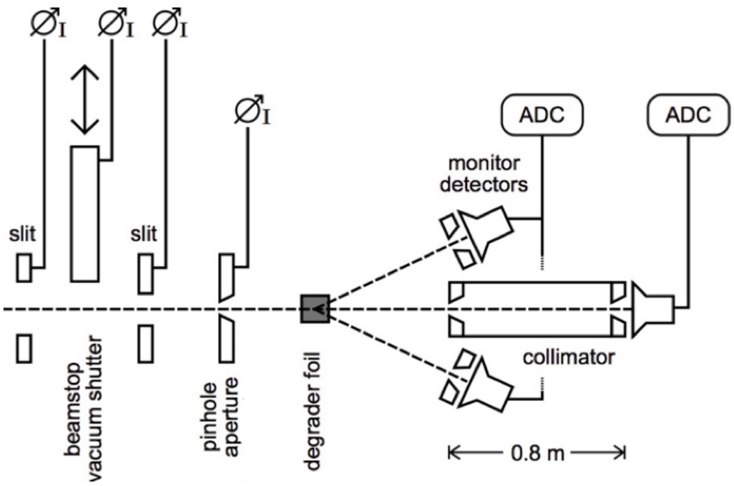

Figure 14 To determine the incident flux on the target, a detector is placed in front of the collimator exit for each beam energy that is used for the measurements. The measured flux on the monitor detectors is set in relation to the incident flux on the target via a normalization parameter.

2.5. Data Analysis Framework

To evaluate the data obtained with the experimental setup (described in Section 2), a data analysis framework has been developed in the object-oriented language C++ based on the analysis framework ROOT[5]. This software has been extended to be able to evaluate on- and off-axis data with three as well as four (or for future measurements – possibly more) detectors. Several input structures have been simplified. Measurement parameters such as detector position or detector channels just need to be typed into a file and the code wraps all the read-in data in compact tree formats. For simplification of the software handling, several parameters like beam energy, mirror and detector positions and so forth are read-in via external input files. E.g., there is an input file to map ADC channels to the detectors with corresponding detector types (central, off-axis, monitor and pulser), integration limits for the spectra of each detector, the aperture diameter of the detectors and the relative position of the detector (from the central detector).[6] The input files help avoiding a code adjustment with every update of the experimental setup, e.g. when ADC channels are connected to different detectors or the number of detectors has changed.

The data analysis procedure to calculate and plot scattering efficiencies is shown in Fig. 17. The DAT files contain spectra for each detector and each run. Together with the input files containing measurement parameters, ADC channel-to-detector mapping, calibration and angle information the first function creates a dataset with run, flux and angle information using the associated classes and stores it into a ROOT formatted file. The drawing function first calculates the scattering efficiencies for each data point per detector (on- and off-axis). The efficiencies for

[5] `https://root.cern.ch`

[6] An example of the input file for the ADC channel-to-detector mapping is shown in the appendix A, Fig. 39.

all detectors will be plotted as a function of the scattering angles. A Firsov or Remizovich function for the on- and off-axis detectors can be added to the plots (for information on Firsov's and Remizovich's scattering descriptions, see Sections 1.2.2 and 1.2.3).

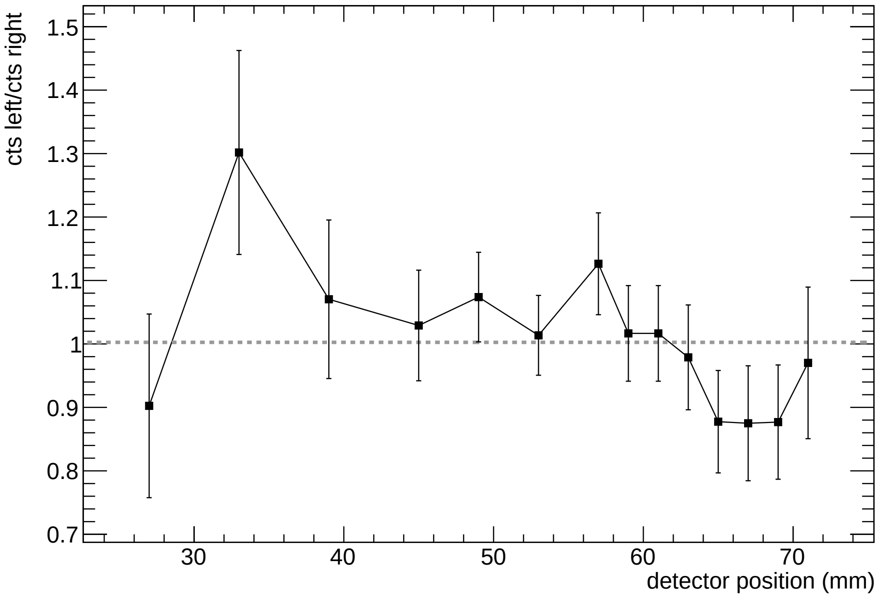

Figure 15 Plot showing an example of the ratio between the off-axis detectors in relation to the detector position from the center for 300 keV proton energy and a mirror position of 66.3 mm. The grey dashed line shows a linear fit which is compatible with one. If the points are not compatible with one within statistical uncertainties as seen here, the alignment of the detectors with the beam need to be reviewed.

For a first and quick overview over the data an express consistency check has been developed. Spectra can be viewed – without normalization and energy calibration – and two graphs are calculated: The ratio between the off-axis detector counts in relation to the detector position to check if the protons are scattered equally to the left and right (see an example in Fig. 15) and the ratio between the two off-axis detectors and the on-axis detector (example shown in Fig. 16). If the ratio between left and right is not compatible with one or the ratio between the central and both off-axis detectors not linearly decreasing, the alignment of target and detectors needs to be checked.

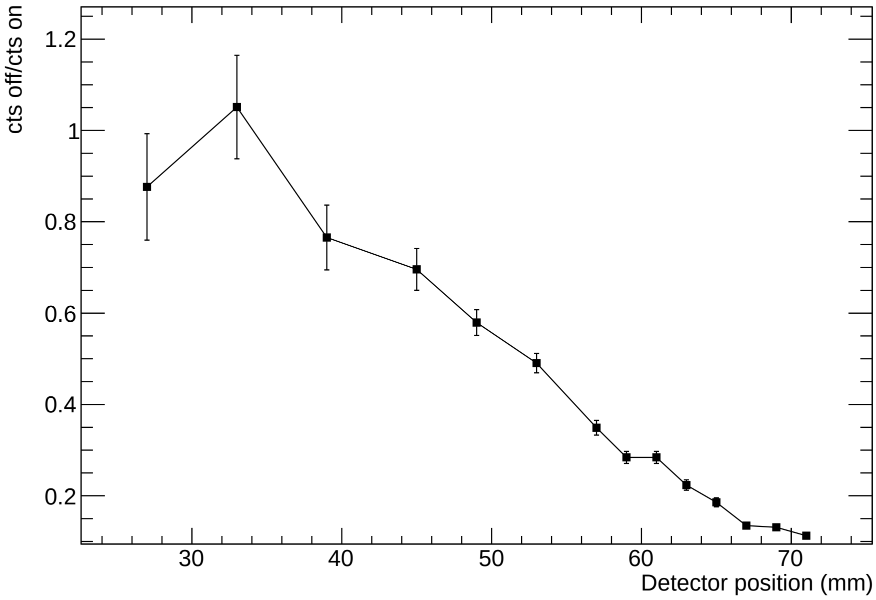

Figure 16 An example of the consistency plot showing the ratio between the two off-axis detectors (averaged counts) in relation to the central detector. The ratio decreases nearly linear which means, that the target and the detectors are well aligned in this example.

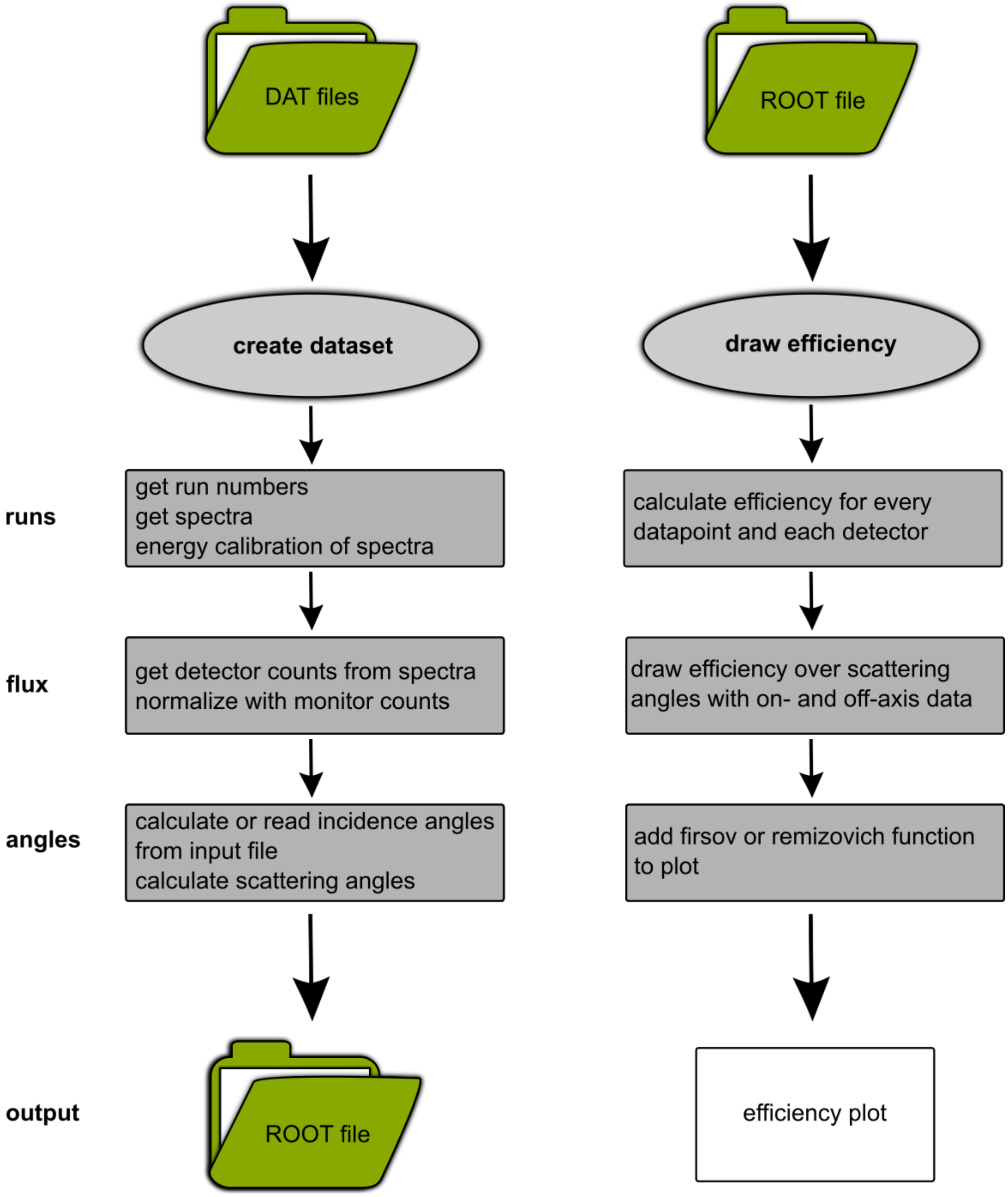

Figure 17 The flowchart shows the data analysis procedure qualitatively. The classes runs, flux and angles which are employed for the steps in the first function to create a dataset are shown on the left. Raw data are stored in DAT files, read in by a function that collects all needed parameters for scattering efficiency calculations. The output data are stored in a ROOT file (respectively tree structures with branches). The ROOT file is used by another function to calculate and draw the scattering efficiency.

3. Studies and Improvements

3.1. Feasibility Study for a Backscattering Detector

The alignment of beam, target and detectors is crucial for the scattering studies as well as the correct normalization procedures. Especially in the case of a curved or thicker scattering target, not all particles are scattered in the forward direction. This effort has to be taken into account for the normalization of the measurements. Backscattered protons can occur if the beam does not hit the target, e.g. at the front end of the mirror sample (see Fig. 18). Most of these protons are stopped in the material, the other very small fraction of protons is scattered back into the direction of the collimator exit and its surroundings.

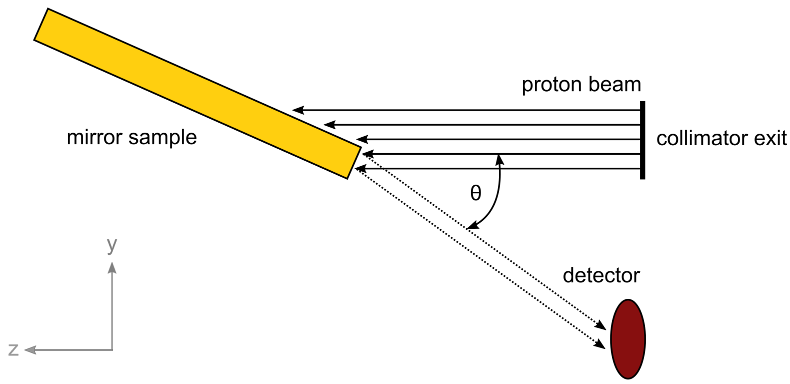

Figure 18 Motivation for the feasibility study: If the beam (black arrows) hits the target (yellow) at the front end there will be particles (dotted black arrows) backscattered into the area underneath the collimator exit under a scattering angle Θ. The study is conducted to see if it is useful to install a backscattering detector (red) and in which distance to the collimator exit it could be mounted.

Therefore, a feasibility study has been conducted to test if there are backscattered protons and furthermore to see if and at which backscattering positions there would be enough flux to install a backscattering detector in the area underneath the collimator exit. For the study, the scattering process has been examined analytically following Rutherford's differential cross section and via a GEANT4 simulation.

Rutherford Scattering

The basic scattering behavior of charged particles interacting via coulomb forces can be described via Rutherford's differential cross section (see Eq. 8). The equation sets scattered particles per solid angle $d\Omega$ in relation to the incoming beam particles and the scattering centers.

$$\frac{d\sigma}{d\Omega} = \frac{\text{backscattered particles (per time) per solid angle } d\Omega}{\text{beam particles (per time)} \cdot \text{scattering centers (per area)}}$$
$$\frac{d\sigma}{d\Omega} = \left(\frac{1}{4\pi\epsilon_0} \cdot \frac{Z_1 \cdot Z_2 \cdot e^2}{4E_0}\right)^2 \cdot \frac{1}{\sin^4(\frac{\theta}{2})} \tag{8}$$

For the purposes of this study the Rutherford formula in nuclear units and in the center of mass system will be used (see Eq. 9), where Z_1 is the charge of the scattered particles, Z_2 is the charge of the nucleus, E_0 is the incoming energy in MeV of the scattered particles respectively the beam, θ is the scattering angle and the cross section is given in units of barn ($1\,\text{barn} = 100\,\text{fm}^2$).

$$\frac{d\sigma}{d\Omega}[\text{barn}] \approx 1.3 \cdot 10^{-3} \cdot \left(\frac{Z_1 \cdot Z_2}{E_0[\text{MeV}]}\right)^2 \cdot \frac{1}{\sin^4(\frac{\theta}{2})} \tag{9}$$

Two different materials have been tested for their backscattering behavior: Silicon as it is also used for the Silicon Pore Optics (SPO) of *ATHENA* and nickel as it is used as a substrate for the *eROSITA* mirrors. Fig. 9 shows the Rutherford formula calculated for both materials. In each case the backscattering probability for a particle falls rapidly for increasing scattering angles. The graph approximates zero even faster for silicon than for nickel, because of a lower charge Z_2 for silicon.

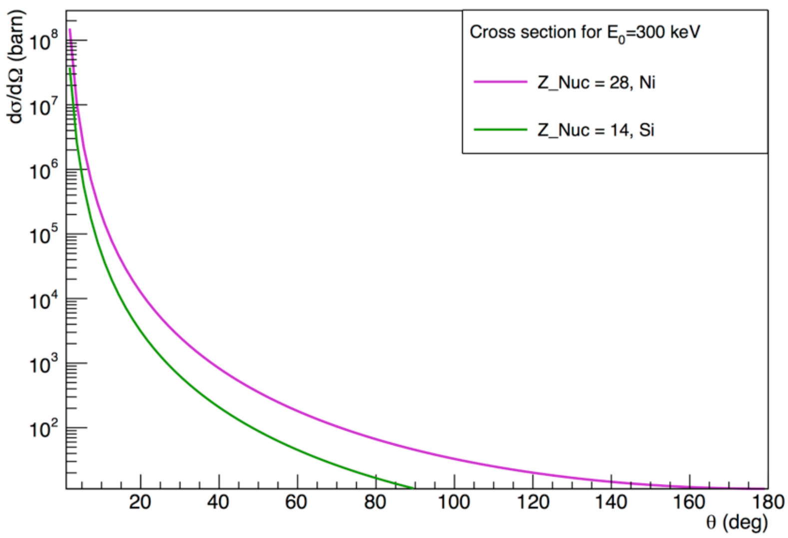

Figure 19 Differential Rutherford cross section as a function of the scattering angle θ for nickel (violet) and silicon (green) for a beam energy of 300 keV following the scattering description after Rutherford given in Eq. 9.

Simulation geometry

To investigate possible count rates on a detector mounted in different backscattering angle positions, a simplified setup geometry as seen in Fig. 20 has been implemented in a GEANT4 simulation [37].
The lower semicircle of the detecting volume in pink represents the area where a backscattering detector with a sensitive area of 8 mm could be mounted in the experimental setup. To simplify the geometry, a whole circle with a radius r = 100 mm and thickness z = 1 mm was used and a cut was applied for data analysis. Having no secondary particles as well as energy loss effects caused by different detector materials, the detecting volume was implemented with "no material" (vacuum).

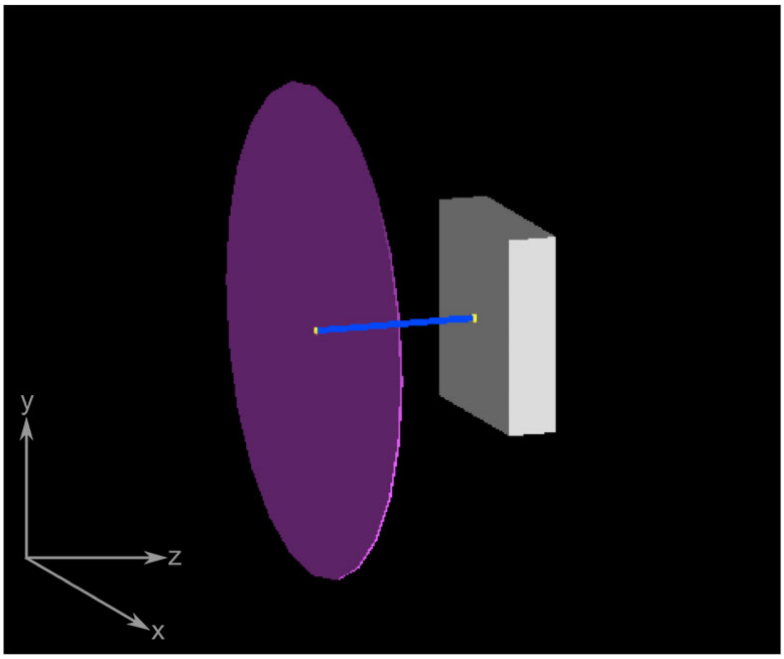

Figure 20 Screenshot of the backscattering simulation in GEANT4: The lower half of the pink circle detecting volume (with radius r=100 mm and thickness z=1 mm for the full circle) represents the area in which a detector could be mounted in the experimental setup to detect protons that are backscattered off the mirror target. The detecting volume consists of "no material" (vacuum). A grey block target (with a size of 40 × 40 × 10 mm) consisting of silicon or nickel has been used to simulate materials corresponding to *ATHENA* or *eROSITA* mirrors. The proton particle source is seen in blue and the yellow dots correspond to interaction areas between particles and material.

The size of the grey target block (40 × 40 × 10 mm) has been chosen large enough to cover the whole beam area and, therefore, to maximize a possible backscattering. Simulations have been calculated with two exemplary mirror materials (silicon and nickel) which are represented by the backscattering block: Silicon as in the silicon pore optics that are used to focus X-rays in case of the *ATHENA* [38] mission and nickel which was used as a substrate e.g. for the *eROSITA* mission and where also measurements have been taken using the experimental setup at the accelerator

facility.
Proton beam energies of 300 keV and 400 keV with 10^{12} particles for each run have been used to simulate the backscattering behavior of protons in case of the two implemented materials. Furthermore, the particle source starts 6 mm behind the detecting volume in z-direction to exclude the counting of particles that would pass through the detecting volume if the source would have been set in front of the volume. In Fig. 20 particles are colored in blue and interaction areas in yellow.

Results

Fig. 21 shows the simulation results for the beam energy of 300 keV and 10^{12} particles per run.[7] The pixels show the counts in the x-y-plane and each pixel has a size of 8 $\times$ 8 mm which corresponds roughly to the sensitive area of an SSB detector (with diameter d = 8 mm) used in the scattering measurements. The circle center is equivalent to a 180° scattering angle.

Most of the backscattered particles hit the detector volume in the center and particle counts decrease in the direction of the circle edge which is quite the opposite behavior as expected following the Rutherford backscattering description (Fig. 19). The larger the backscattering angle the more particles are scattered towards the detector.
The backscattering probability for a particle is around 10^{-9} per solid angle corresponding to the simulation results from GEANT4 and around 10^{-7} when cross-checked with the SIMNRA[8] software [39]. The difference in the order of two magni-

[7] For completeness the results for 400 keV can be found in the Appendix (see Section B.1). The number of backscattered particles for this energy is even lower than for 300 keV so that the plots indicate the same result as it is stated in this section.

[8] SIMNRA is a program for the simulation of backscattering spectra incident beam ions from about 100 keV up to many MeV. It can be used to simulate different backscattering processes, e.g. Rutherforn backscattering or elastic backscattering.

tudes is still an unsolved matter of discussion. Yet, in both cases the backscattering probability is very low.

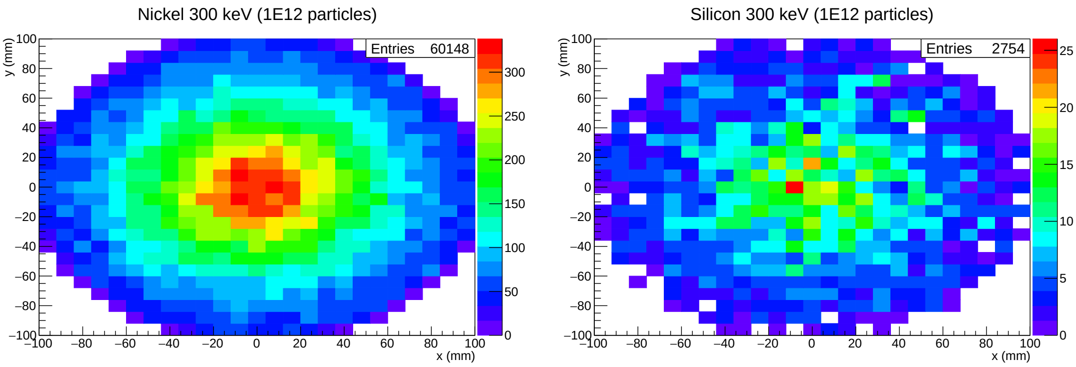

Figure 21 The two-dimensional scattering distributions of simulated backscattered protons in the area of the detecting volume in the cases of nickel (left) and silicon (right) for a beam energy of $E_0 = 300\,\text{keV}$. Each pixel corresponds to the sensitive area of a silicon surface barrier detector (with a diameter d = 8 mm) used in the actual experimental setup to detect scattered particles.

The scattering description following Rutherford is not sufficient to describe the physics of backscattering at thick targets, like the ones tested in this study. The Rutherford cross section is valid for thin targets such as a gold foil used in the Rutherford experiment (about 1000 atomic layers) where the particles are scattered at the nuclei of the gold foil and backscattered following the Rutherford scattering formula. Concerning the backscattering process for thick targets further interactions need to be taken into account, e.g. energy loss of particles and therefore different backscattering behavior of the particles, secondary particles, absorption, combinations of elastic and inelastic scattering (on scattering processes at thick targets cf., e.g. [40], and [41]). For an extensive analysis, it would be of use to consider further Monte Carlo Simulations or the SIMNRA software for the simulation of backscattering processes.

As a result of this study, no additional backscattering detector was mounted in the experimental setup due to the extremely low flux rates on this detector and the low probability for backscattered protons towards the measurement device.

3.2. Off-axis Detectors

The detector configurations to measure scattered protons at the end of the beamline have been extended two times and tested. Both extensions were made to gather information about the azimuthal scattering distribution of protons.

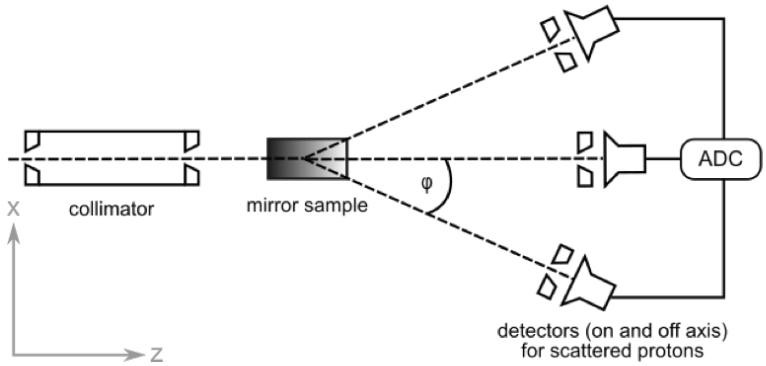

Figure 22 Schematic view of the experimental setup with two additional off-axis detectors from above (x-z-plane). The beam enters from the left in the positive z-direction, passes the collimator and particles are scattered off the mirror surface towards the three detectors. These detectors are mounted at the same distance corresponding to an angle φ in relation to the detector in the center.

For the first extension, three SSB detectors instead of only one have been mounted in a row with the central detector (see Fig. 22). The off-axis detectors on the left and right are installed at a distance of 32 mm to the central detector, which equals azimuthal angles of $\varphi = \pm\, 2°$.

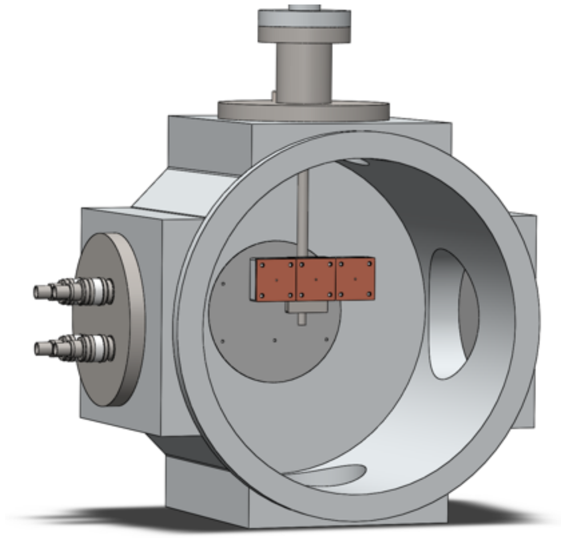

Figure 23 The CAD graphic shows the front view on the three detectors mounted in a row in the experimental setup with surrounding detector chamber and cable connections on the left side [29]. To scan the scattering angles, the detector array is moved by a linear manipulator. The off-axis detectors on the left and right are installed at a distance of 32 mm to the central detector, which equals azimuthal angles of about $\pm$ 2°.

The CAD model in Fig. 23 shows the mounting of the detectors in an array in the detector chamber at the end of the beam line. All three detectors are adjustable via a manipulator from above. The detector chamber has a diameter of 250 mm so that the maximum scattering angle with the detector array is limited to about 4° [29].

For the second extension four detectors have been installed in an array – a mixture of one SSB off-axis detector and three passivated implanted planar silicon (PIPS) detectors. The fourth detector for the second extension is mounted additionally and not displayed in the CAD model but shown in the scheme in Fig. 24. It is installed at a distance of 64 mm to the central detector which corresponds to an azimuthal angle of about 4°.

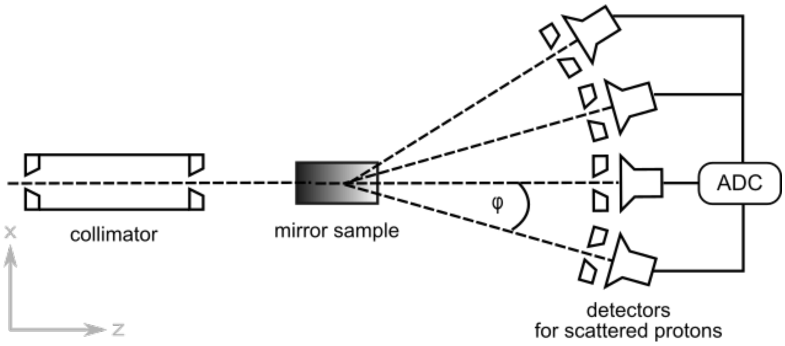

Figure 24 Same as in Fig. 22 but with a fourth detector at a distance of 64 mm to the central detector which corresponds to an azimuthal angle of about 4°. There are three PIPS detectors (from top to bottom) and the one on the bottom is an SSB detector.

3.3. Detector Studies (SSB and PIPS)

For the measurements with four detectors – one SSB, three PIPS – the noise of the devices has been studied. The studies were carried out in the course of the scattering efficiency measurements to determine the lower energy limit of the PIPS detectors, and to determine the signal-to-noise ratio of the detectors. Pure noise measurements have been taken with the accelerator turned off before and after the scattering measurements. All runs shown in, e.g. Fig. 25 have been taken at diffferent detector positions to measure the scattering efficiency and are also used for the noise studies. The beam-on measurements have been taken with an energy of 1002 keV.

The detector counts have been normalized to the data acquisition time using the pulser counts. Since two ADCs with four channels each are used, a pulser signal is fed to each of the ADCs to account for possible dead times. For the normalization of the detector counts, the respective pulser was used.

In Fig. 25 the pulser counts of both pulsers are presented for each run. The pulsers are running at a frequency of 55 Hz. Therefore, their counts are proportional to the measuring time.

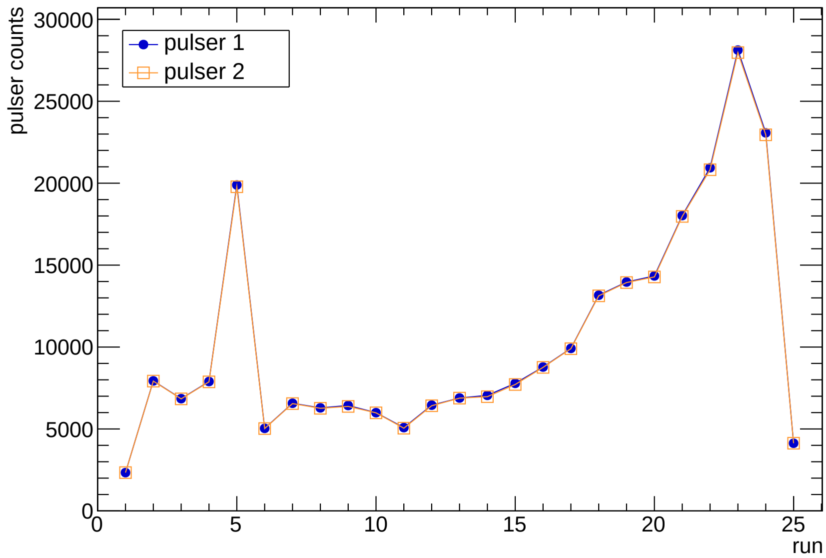

Figure 25 Plot showing the pulser counts of both pulsers (blue and orange) for all runs that are used to study the noise of the detectors. The pulser counts are proportional to the measuring time. The first run is a noise-only measurement as is the last – for both noise runs the accelerator has been turned off.

The first (run 1) and the last run (run 25) are the noise measurements without beam. The increase of pulser counts in between the second and the penultimate run reflects an increased measuring time. The measuring time is prolonged as there are fewer detector counts (in particular on the off-axis detectors) with increasing detector position (which equals larger scattering angles). Hence, the decreasing of the detector counts is compensated with an increase of exposure time of the detectors for the larger scattering angles.

Fig. 26 demonstrates the dependency of the noise on the data rate for all four detectors: For the PIPS detectors on the central and azimuthal positions of $\varphi = 0°$,-1.98°, -3.96° as for the SSB mounted at $\varphi = +1.98°$. At low ADC counts, the data is dominated by noise. In order to lower the energy limit in the scattering efficiency measurements as far as possible, the possibility to subtract the noise contribution using a reference noise run was studied.

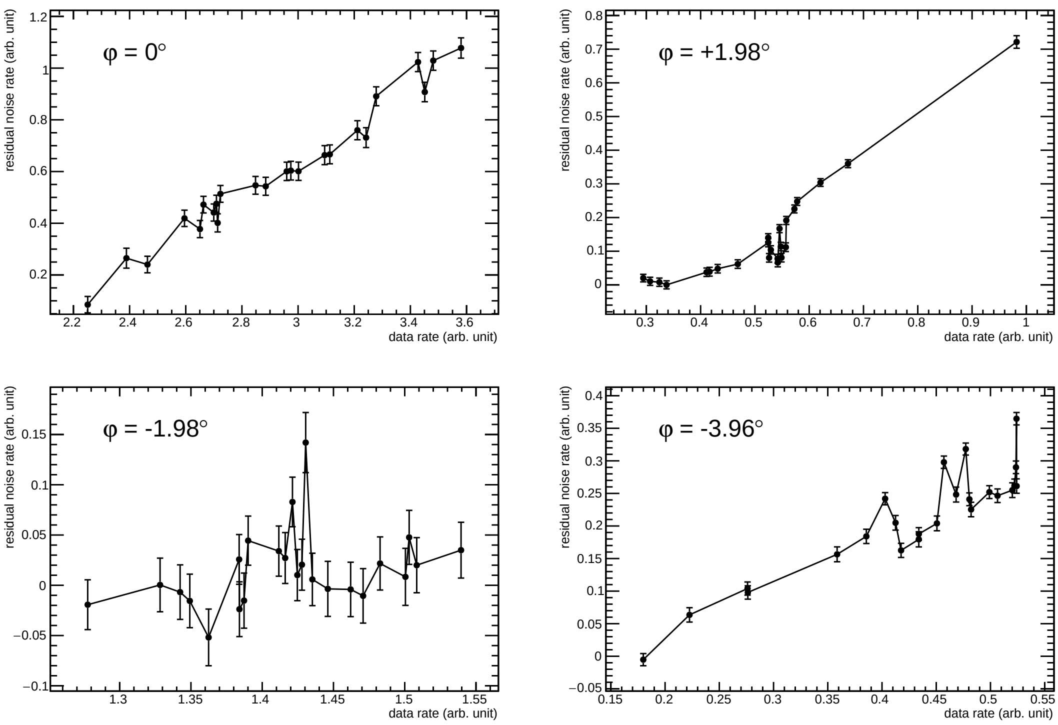

Figure 26 The four graphs show the residual noise rate (for details see text) depending on the data rate for the central detector at the azimuth position $\varphi = 0°$ (top left), the off-axis detector on the left at $\varphi = +1.98°$ (top right), the off-axis detector on the right at $\varphi =$ -1.98° (bottom left) and the off-axis detector on the very right at $\varphi =$ -3.96° (bottom right). The detectors in the central position, on the right and very right – at φ = 0, -1.98, -3.96° – are PIPS detectors. The detector at $\varphi = +1.98°$ is an SSB detector.

To test the possibility to subtract the noise contribution, data from the scattering measurements have been normalized to the data taking time using the pulser counts (see Fig. 25) as an estimate. Thus, the count rate per ADC channel is obtained. The same was done for the first noise run and then subtracted from the

normalized data spectrum. The residual spectrum was then integrated in the noise region. This value gives the residual noise rate – the noise which is not subtracted via this method. In Fig. 26 the residual noise rate as a function of the data rate is presented. The data rate is obtained by dividing the total detector counts by the pulser counts.
For three detectors Fig. 26 shows, that the noise increases as the data rate also increases. The only detector which shows a reproducible noise behavior and nearly no dependency on the data rate is the PIPS detector on the right at φ = -1.98°. The noise shows a slight increase with the data rate but stays nearly constant within the calculated statistical uncertainties. The underlying noise spectra of the total noise counts in Fig. 26 as well as the residual noise spectra can be seen in the Appendix (B.2, Fig. 41 and Fig. 42).

In Fig. 27 the spectra of a PIPS and an SSB detector are presented. The spectra have been measured at a primary beam energy of 1001 keV corresponding to a Gaussian proton spectrum of 193 keV with a FWHM of 68 keV after the copper degrader foil[9]. The signal is fitted with a Gaussian function and a reference line has been added at a distance of -3 σ from the mean in the same color as the fit. This line is used as a maximum for the lower signal count integration limit in order to minimize the error on the signal counts. A red reference line is added at a position around the upper noise limit at which the value of the data counts at the -3 σ line of the signal is the same as in the area of the noise drop. In a last step, the distance between the two reference lines has been measured for a comparison of the signal-to-noise ratio.

[9]The spectrum was obtained by using TRIM and is shown in the Appendix C.1, Fig. 43.

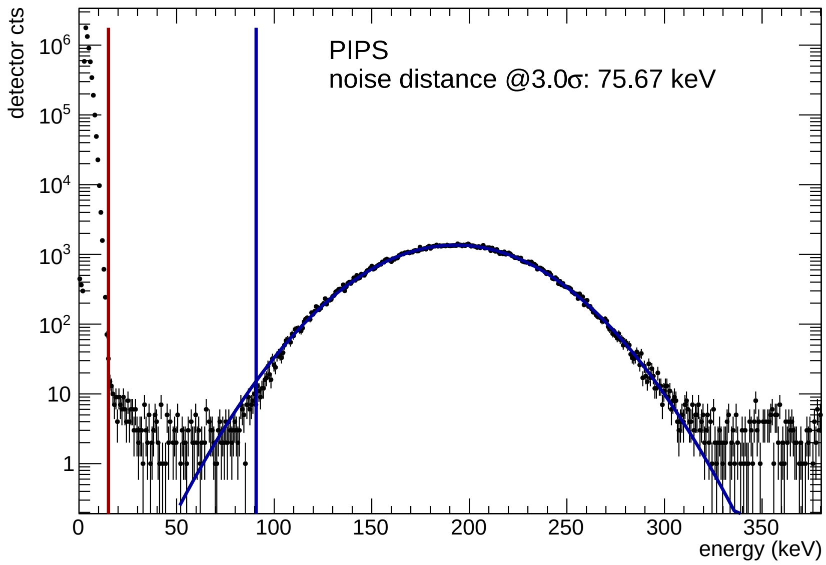

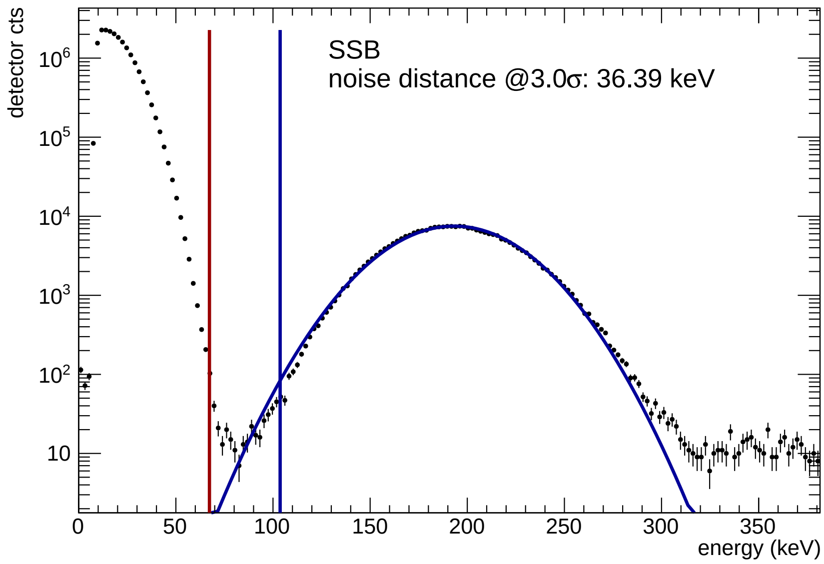

Figure 27 Spectra of a PIPS (top) and an SSB detector (bottom) with Gaussian fitted signal in blue and a blue reference line at a distance of $3\,\sigma$ of the mean value. A red reference line has been added at the position with the same data count value as the blue reference line. The distance between the two reference lines shows that the PIPS detector has a much better signal-to-noise ratio than the SSB. The distance between the reference lines of signal and noise in the SSB spectrum is more than half the length as in the PIPS spectrum.

A coarse energy calibration was applied to the detector. This was done using a linear scaling between ADC counts and energy. It was assumed that zero ADC counts correspond to 0 keV without static offset and the mean of the Gaussian fit to the spectrum to the estimated beam energy after the foil, 193 keV, as stated above.
Fig. 27 shows that the distance between signal and noise of the PIPS detector is more than twice the distance found in the SSB spectrum. Hence, the signal-to-noise ratio is about a factor of two better for the PIPS than for the SSB detector.

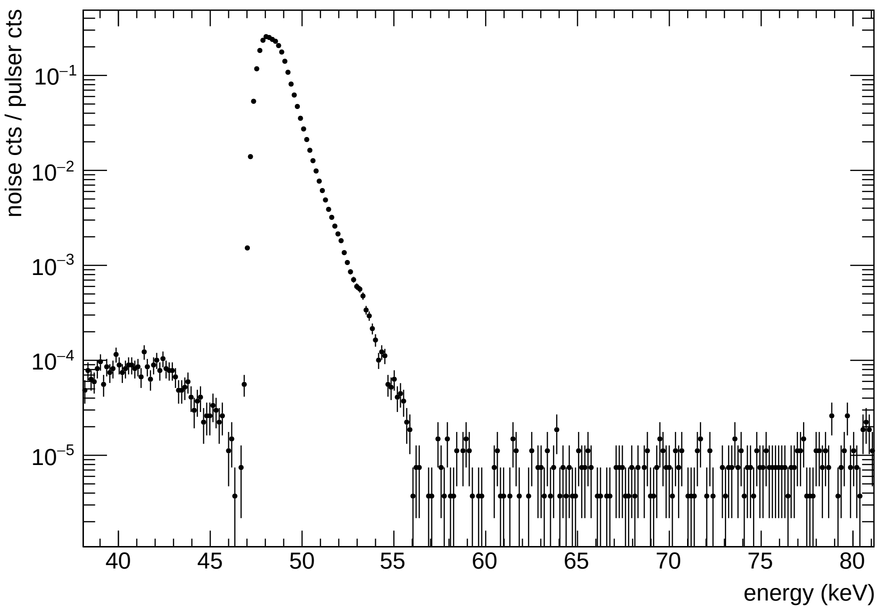

Figure 28 Plot showing the energy threshold of the noise. All spectra of the noise measurements have been summed and divided by the number of pulser counts of the central PIPS detector. The lower energy threshold of the PIPS detectors can be found in the region of 50-60 keV.

In Fig. 28 is the calculation of the lower energy threshold of the central PIPS detector presented which was energy-calibrated via TRIM (see Section 3.4). All spectra of the noise measurements have been summed and divided by the number of pulser counts. As shown in Fig. 28 the noise of this specific detector reaches about 50-60 keV. The value is around 40-50% lower than estimated for the SSB detectors where the noise extends up to 80-100 keV (cf. [23]).

In conclusion, the noise contribution is not stable, but depends on the data rate. Therefore, it is not easily possible to subtract the noise from the measurement. Instead a low energy cut needs to be applied to the spectra for the analysis. For three out of four detectors, the noise increases with a rising data rate independent of PIPS and SSB detector type. Only the PIPS detector at φ = -1.98° showed a steady noise behavior within statistic uncertainties. The PIPS detector which was investigated in Fig. 27 has a much better signal-to-noise ratio than the SSB detector. Furthermore, the lower energy threshold of the PIPS detectors was located in the region between 50-60 keV.

3.4. Energy Calibration via TRIM

The calibration procedure using the Rutherford backscattering (RBS) method (see Section 2.4) is very time consuming since the detectors have to be moved to another chamber. Furthermore, the analysis of the calibration is not trivial due to e.g. the multiple fit routines. A calibration method via TRIM-simulated spectra is much more efficient and has the additional advantage that the calibration is done in the energy range of interest.
For this calibration method, two spectra have been measured with the detectors of the experimental setup for two different degrader materials, e.g. a 6 μm copper foil and a 10 μm aluminum foil and without a target in the course of the beam. The measured spectra have been fitted with a Gaussian function to extract the mean of the distribution in ADC counts as shown in the top two panels of Fig. 29.

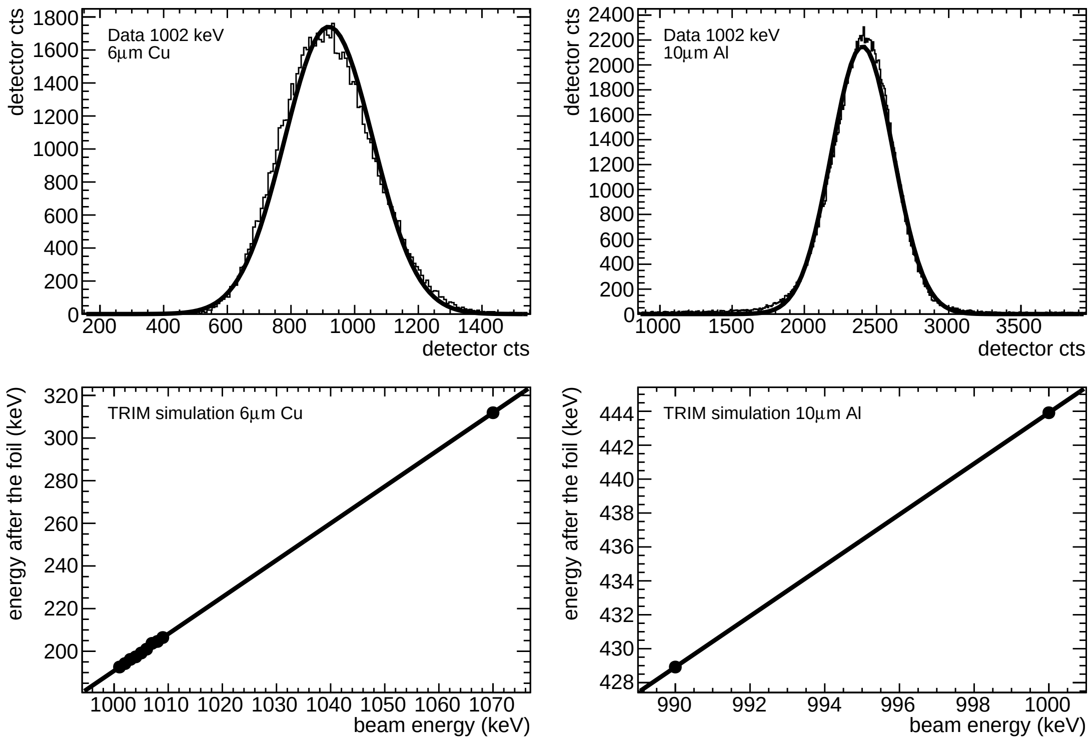

Figure 29 Measured spectra without target for a primary beam energy of 1002 keV behind a 6 µm copper degrader foil (top left) and a 10 µm aluminum foil (top right), respectively. The energy after the degrader foils using a TRIM simulation are shown as a function of the primary beam energy in the bottom plots. A cut for exit angles $\pm$ 3° has been applied on the simulated spectra to only select protons in the direction of the detector.

Additionally, the energy spectra behind the degrader foil have been simulated for several beam energies using TRIM (see example plots in the Appendix C.1). A cut for exit angles $\pm$ 3° has been applied on the simulated spectra to only select protons in the direction of the detector. The resulting spectra were also fitted with a Gaussian function and the mean of the energy distribution is related to the initial beam energy (see bottom two panels of Fig. 29).

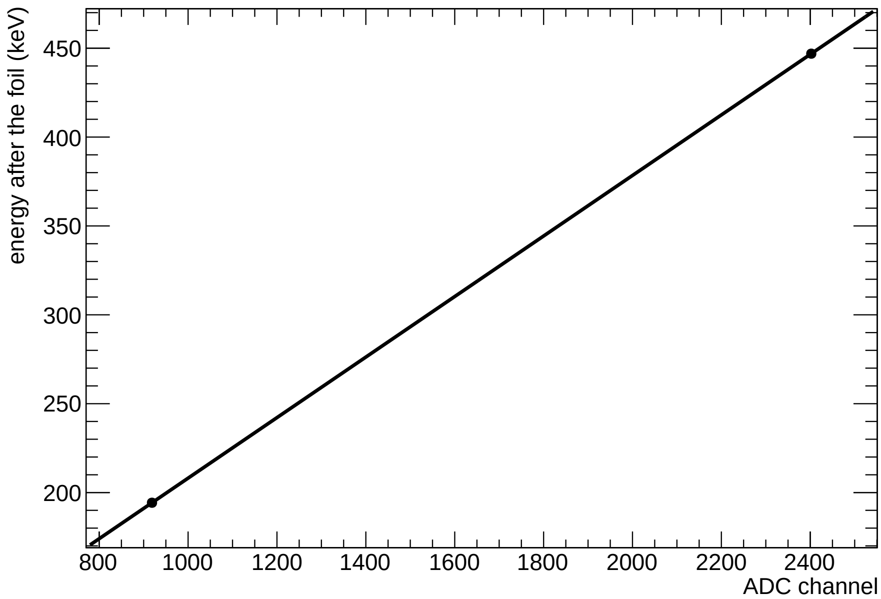

Figure 30 Detector calibration curve relating the ADC counts measured by the detector with the energy behind the degrader foil as simulated by TRIM. A linear scaling is assumed.

For the detector calibration, the extracted ADC values for the two degrader foils are set in relation to the proton energy behind the degrader foil as extracted from the TRIM simulation. A linear scaling is assumed as shown in Fig. 30.
To cross-check the calibration, in Fig. 31 the energy-calibrated data spectrum is overlaid with the spectrum obtained by the TRIM simulation. The measured spectrum is slightly narrower than the TRIM spectrum. A possible reason could be that the opening angle of the detector ($\sim 0.03°$) is two orders of magnitude smaller than the opening angle cut used for the TRIM simulation ($\pm$ 3°). For the conducted simulations, a tighter cut could not be applied due to the limited statistics available.

In the future, it might be interesting to test the dependence of the energy distribution of the TRIM simulation on the opening angle cut using more statistics.

Also, the TRIM calibration method needs to be compared to the RBS calibration principle in order to prove a possible equality in the calibration quality. Currently, not enough measurements are available with comparable energies or sufficient measurements for an interpolation of both calibration methods.

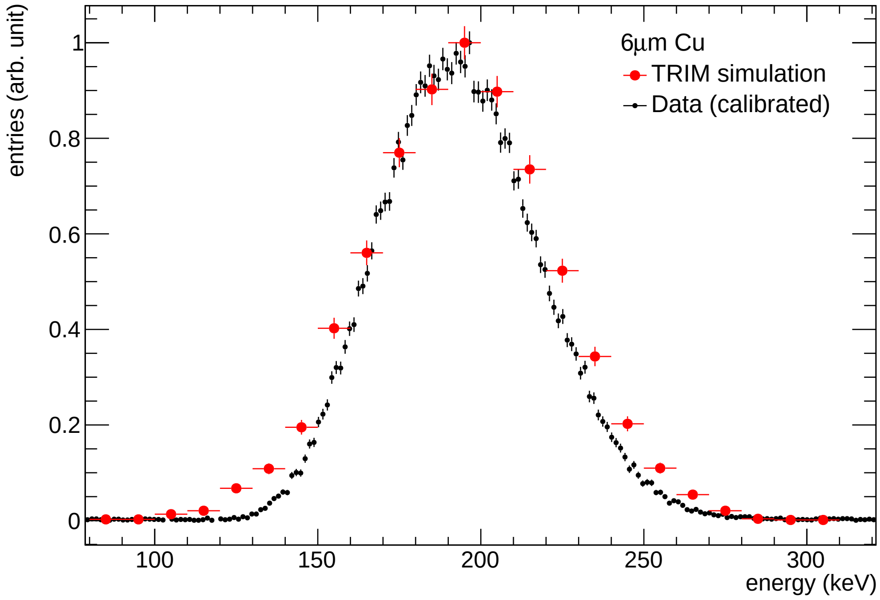

Figure 31 Measured spectrum (black) after energy calibration and TRIM-simulated spectrum (red) for a primary beam energy of 1002 keV and a copper degrader foil with 6 µm thickness. The simulated spectrum is centered around a mean value of 193 keV and FWHM of 68 keV.

4. Results: Grazing Angle Scattering Efficiency Measurements

Two quantities – the scattering efficiency and the most probable energy loss – can be inferred from the measurements. The scattering efficiency η is calculated by dividing the detected number of protons N_{det} for a specific incidence angle Ψ and scattering angle Θ by the number of incident protons N_{inc} on the scattering target. Furthermore, the scattering efficiency is normalized to the solid angle Ω of the detector. The solid angle depends on the scattering angle Θ and on the azimuth angle φ (see Eq. 10).

$$\eta(\Psi,\Theta,\varphi) = \frac{\Phi_{\text{det}}(\Psi,\Theta,\varphi)}{\Phi_{\text{inc}}}\frac{1}{d\Omega} = \frac{N_{\text{det}}(\Psi,\Theta,\varphi)}{N_{\text{inc}}}\frac{1}{\Omega(\Theta,\varphi)} \tag{10}$$

To calculate the most probable energy loss ΔE the main peaks of the incident spectrum and also of the measured scattered spectrum are fitted with a Gaussian. The most probable energy loss results is then the difference of the means μ of the fits (see Eq. 11).

$$\Delta E(\Psi,\Theta,\varphi) = E_{\text{inc}} - E_{\text{det}}(\Psi,\Theta,\varphi) = \mu_{\text{Gauss,inc}} - \mu_{\text{Gauss,det}}(\Psi,\Theta,\varphi) \tag{11}$$

For the off-axis measurements, the scattering efficiency has been evaluated with three or four detectors, respectively. The measurements have been conducted for a different beam energies and have been repeated using another beam energy. The energy loss has not been evaluated in the context of this work. It has been studied in preceding measurements (see [23]).

Off-Axis Adjustments of Solid Angles

The scattering efficiencies are normalized to the solid angle Ω. The calculation of the solid angles of the off-axis detectors has been added to the analysis framework (which is explained in Section 2.5). Fig. 32 shows a scheme with all the variables that are used for the calculation. The solid angle is defined as

$$\Omega = \frac{A_{\text{det}}}{d'^2} \tag{12}$$

with

$$\begin{aligned} A_{\text{det}} &= \pi \cdot \left(r_{\text{det}} \cdot \cos(\Theta)\right)^2 \\ \Theta &= \operatorname{atan}\left(\frac{h'}{d_{\text{det}}}\right) \\ h' &= \sqrt{(y_0 - y_{\text{pos}})^2 + x_{\text{rel}^2}} \\ d' &= \frac{d_{\text{det}}}{\cos(\Theta)} - \sin(\Theta) \cdot r_{\text{det}} \end{aligned}$$

where A_{det} is the detector area, r_{det} the radius of the detector aperture (an effective radius with angular correction, marked in green in Fig. 32), Θ the scattering angle (in the y-z-plane), height of the off-axis detectors h' equals h for $\text{x}_{\text{rel}} = 0$ (on-axis detector position), y_{pos} the detector position (the larger the scattering angles the smaller are the manipulator values for this position), y_0 the detector position where the target is completely out of the beam course, d' the distance from target to off-axis detector, and $d_{\text{det}} = 933\,\text{mm}$ the distance between target and central detector.

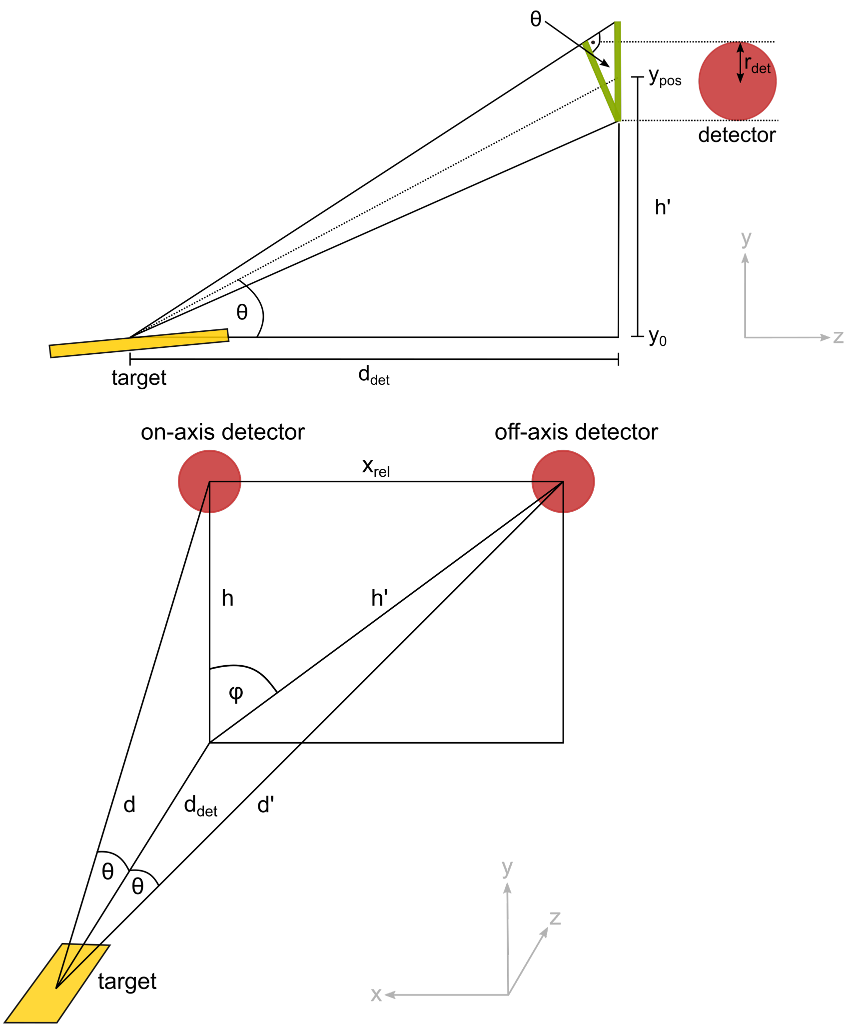

Figure 32 Scheme to illustrate the quantities that are used to calculate the solid angles of on- and off-axis detectors for normalization: Θ is the scattering angle, φ the azimuthal angle, d, and d' are the distances between target and detector, d_{det} is the distance between the target and the null position of the detector, h, and h' is the height between the null position of the detector y_0 and the detector position y_{pos}, r_{det} is the angle-corrected effective radius of the detector and x_{rel} is the relative position of the detectors (in relation to the on-axis detector). The step-by-step calculation of the solid angle (Eq. 12) shows the adjustments for the determination of the off-axis solid angle.

4.1. On- and Off-Axis Measurements with SSB Detectors

For the on- and off-axis measurements with three SSB detectors, a primary beam energy of 1070 keV was selected. After the 6 µm copper degrader foil, the Gaussian proton spectrum has a mean value of about 312 keV with a FWHM of 63 keV.[10] A part of an *eROSITA* mirror shell was used as target. Scattering efficiencies have been measured for three incidence angles of $\Psi = 0.50°$, $0.64°$ and $0.81°$. For each incidence angle data have been taken with an on-axis SSB at an azimuthal position of $\varphi = 0°$ and two off-axis SSBs at $\varphi = \pm 1.98° \pm 0.13°$. The results of these measurements have been published in [29].

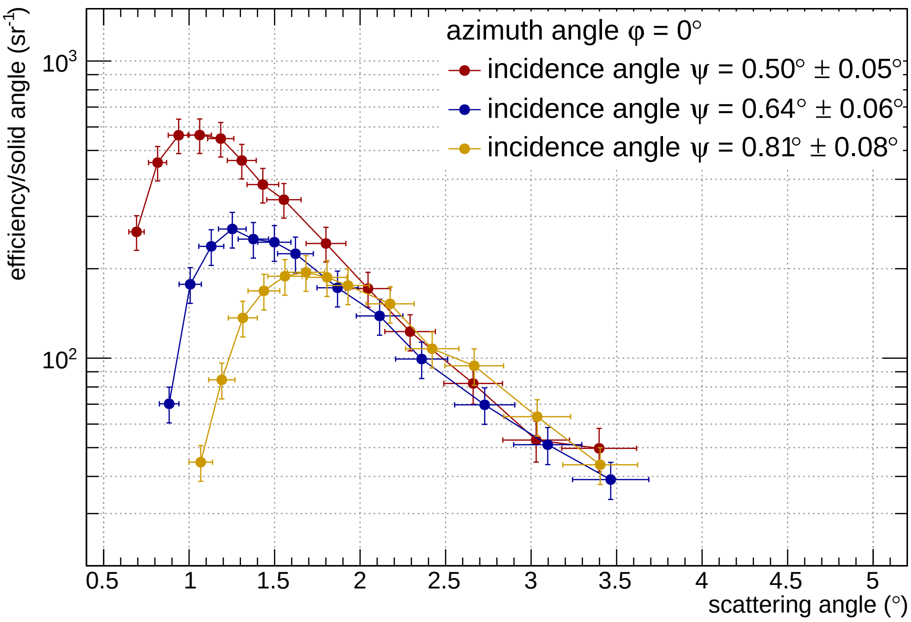

Figure 33 Scattering efficiency for the on-axis detector at the azimuthal position $\varphi = 0°$, for three incidence angles measured with a 312 keV proton beam.

[10]The Gaussian proton spectrum after the foil is simulated via TRIM. Mean and sigma of the distribution are obtained with a Gaussian fit and values are cut on small exit angles of the protons (±3°). The TRIM simulated spectra are shown in the Appendix C.1.

The on-axis measurements are compared in Fig. 33. The maximum scattering efficiency is marginally higher compared to prior measurements but compatible within the calculated errors (published in [23]) and can be found at slightly higher scattering angles than $\Psi = 2\Theta$ which is the condition for specular reflection. The scattering efficiencies in Fig. 33 behave in the same way as the ones in the preceding measurements (shown in [23]): The efficiencies are higher for smaller incidence angles, the efficiencies increase rapidly, reach their maximum around a scattering angle twice the incidence angle and after the maximum the efficiencies decrease fast with respect to the scattering angle. For scattering angles above 2° the scattering efficiency is independent of the incidence angle.

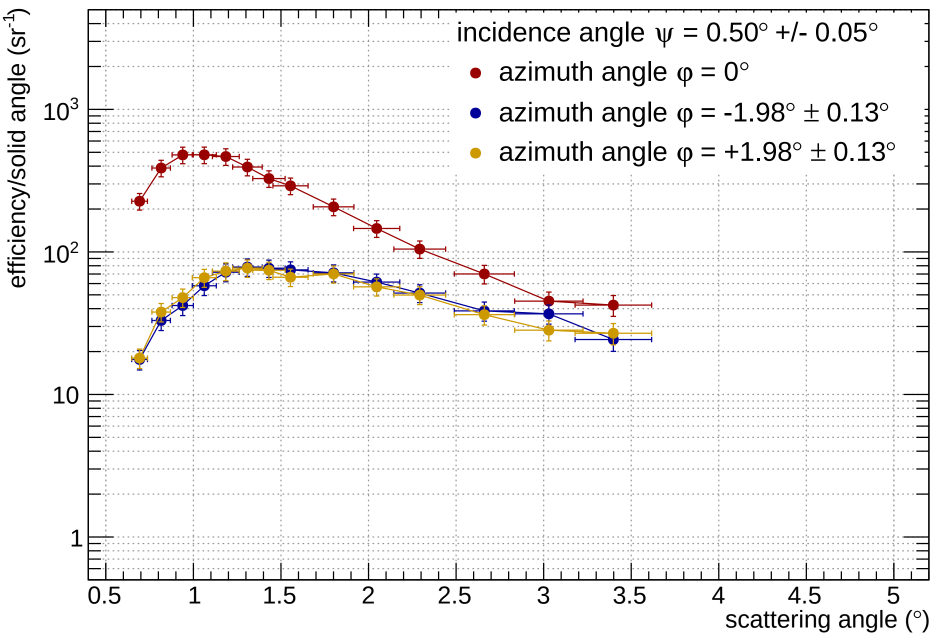

Figure 34 On- and off-axis scattering efficiencies measured for incidence angles of $\Psi = 0.50° \pm 0.05°$ for a proton energy of 312 keV.

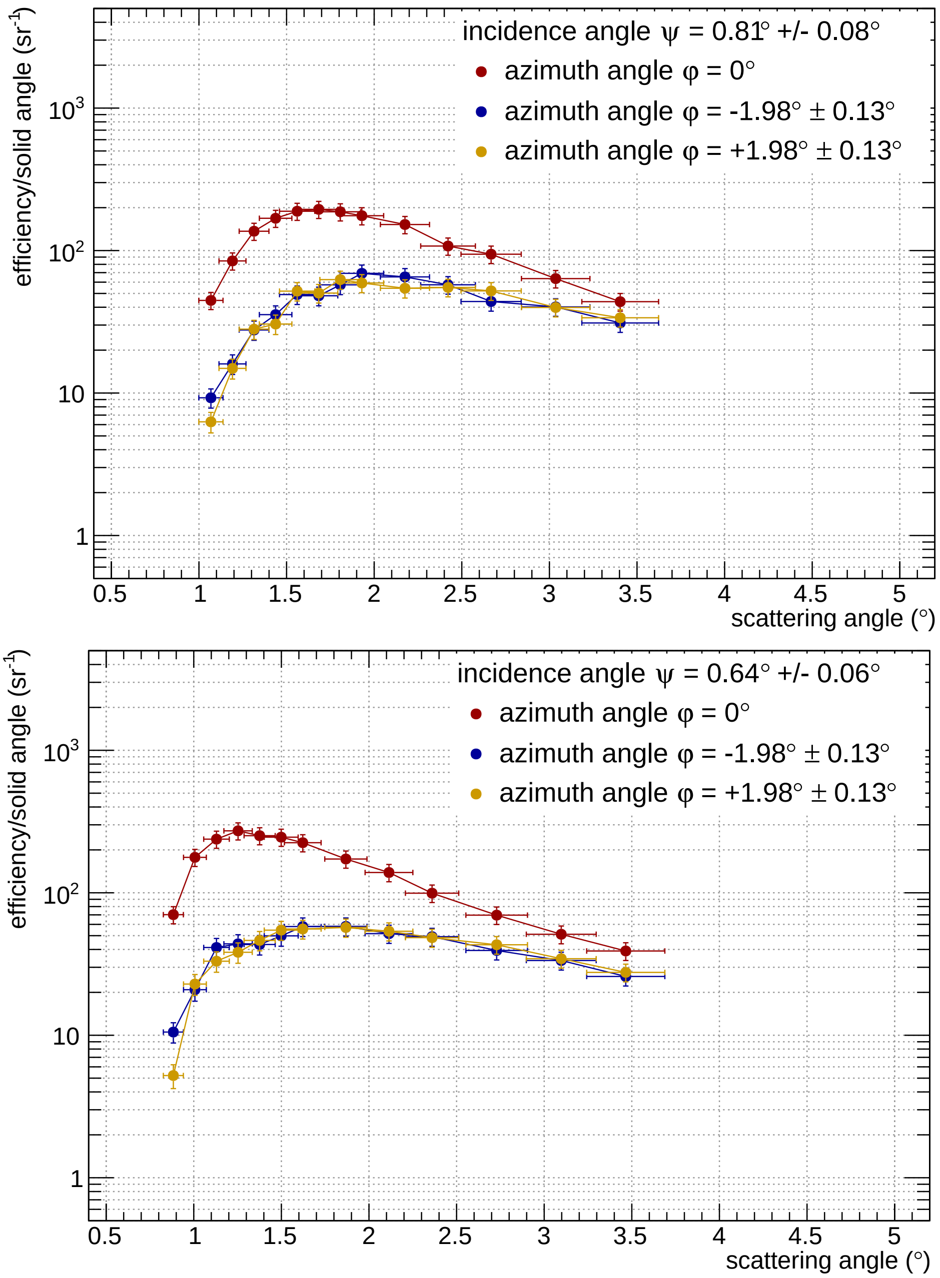

Figure 35 Same as Fig. 34 but for incidence angles of $\Psi = 0.81° \pm 0.08°$ and $0.64° \pm 0.06°$.

Figures 34 and 35 show the off-axis compared to the on-axis efficiencies measured for three incidence angles. The efficiencies of the two off-axis detectors are in a very good agreement.The almost perfect accordance of the off-axis detectors indicates a very good alignment of collimator, target, and the three detectors.

4.2. On- and Off-Axis Measurement with SSB and PIPS Detectors

For the on- and off-axis measurements with one SSB and three PIPS detectors, a primary beam energy of 1002 keV was used. The proton spectrum is centered around approximately 194 keV with a FWHM of 68 keV after the degrader foil. An *eROSITA* mirror shell part was used as a target. Scattering data have been taken for an incidence angle of 0.66° (see Fig. 36). For this measurement, a much finer scan of the scattering angles has been done compared to previous measurement. Additionally, the reach of the scattering angle has been increased by 40% from 3.5° up to 4.5°. For the off-axis detector at φ = -3.96° the last two data points have been excluded since their spectra showed unexpected low count numbers.

In Fig. 36 the efficiency of the on-axis detector reaches its maximum at a scattering angle of ∼1.5° which is more than twice the incidence angle. This could mean that the incidence angle of the beam may be larger than calculated. The plot shows an even better alignment of target, collimator and off-axis detectors than in the measurements shown in Fig. 34. The efficiencies of the detectors at φ = ± 1.98° are nearly identical. Fig. 36 also shows that the efficiencies continue to decrease exponentially after they reached the maximum. This was not clearly deducible from prior measurements (see [23] as well as [29]) due to the lower number of data points adn therefore reach in scattering angle that had been measured. Furthermore, the efficiencies of on- and off-axis detectors at φ = ± 1.98° converge for larger scattering angles. This may be an effect of the decreasing of the azimuthal angle φ with increasing height of the detector array, as the relative dista between the detectors is fixed (deducible from the scheme in Fig. 32).

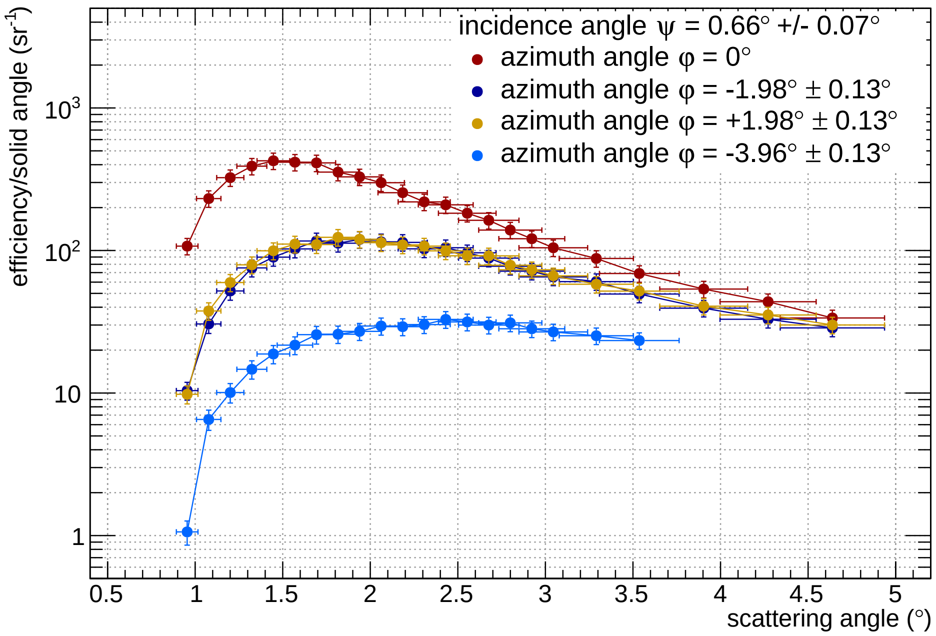

Figure 36 Scattering efficiency for an incidence angle of 0.66°± 0.07° and an incidence energy of 194 keV.

Compared to the prior measurements at 0.64° (see Fig. 34) the efficiencies shown in Fig. 36 are slightly higher although the incidence energy is about 100 keV lower than for the measurements in Fig. 34. This deviates from the findings in [23] where slightly higher efficiencies for larger incident energies have been found. Therefore, the angle calculation and the flux normalization need to be checked for the measurement with an incidence angle of 0.66°, as they affect the scaling of the efficiencies shown in Fig. 36.

4.3. On- and Off-Axis Measurements compared with the Remizovich model

The measured scattering efficiencies for 0.66° with a 312 keV proton beam have been compared to the theoretical model of Remizovich (see 1.2.3) in Fig. 37. The Remizovich function for a certain incidence angle (here: 0.66°) has been integrated over the opening angle of the detector and normalized to the solid angle.

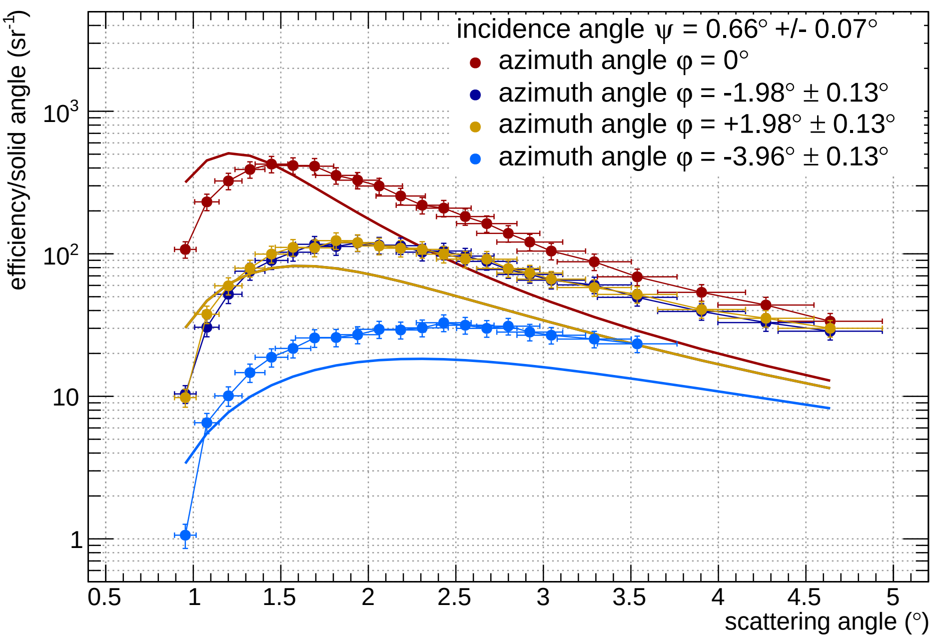

Figure 37 Efficiencies as shown in Fig. 36 with analytical Remizovich functions for on- and off-axis measurements.

The on-axis Remizovich has a much higher maximum than the measured data and the slope decreases faster. For the off-axis detectors at ±1.98° the model fits better but does not describe the data properly. The larger the off-axis angles of the detectors get, the better the match with the Remizovich function. For the second off-axis detector at the largest azimuthal angle of -3.96° the model function

would fit for almost all measured scattering angles.
All Remizovich functions in Fig. 37 are shifted towards smaller efficiencies. A crosscheck has shown that the Remizovich functions for the on- and off-axis detectors match best with the data taken at the incidence angle of 0.66° in case of an incidence angle of 0.85° for the analytical function. This discrepancy has not been solved yet. Maybe the incidence angle of the measurement has been larger than calculated or the normalization of the Remizovich functions has to be adjusted. Also, the flux normalization needs to be carefully checked, as they determine the scaling of the efficiencies.

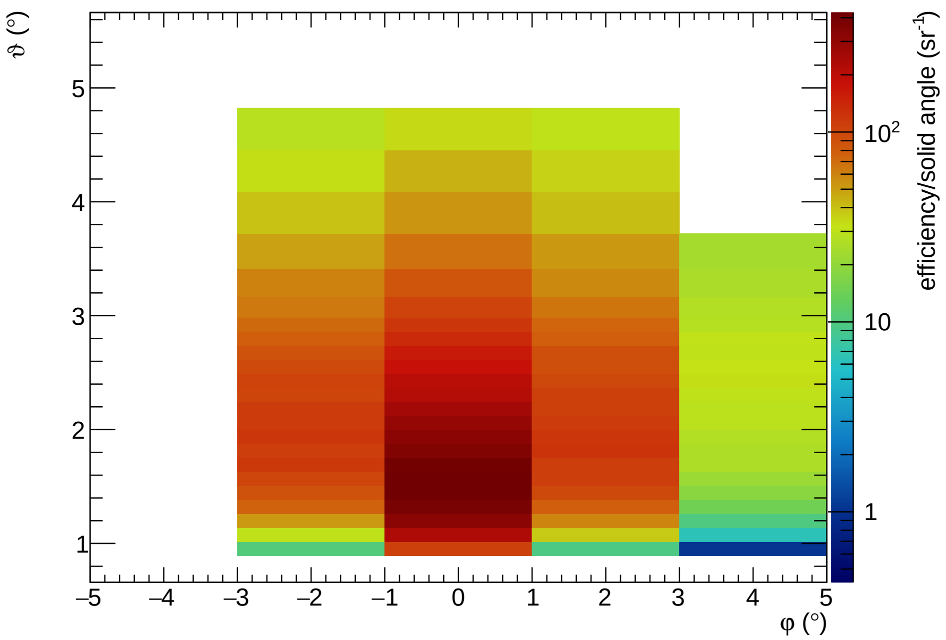

Figure 38 Results as shown in Fig. 36 in a two-dimensional plot of the scattering angle θ in relation to the azimuth angle φ similar to the two-dimensional Remizovich function that has been presented in Fig. 4. The central detector efficiency is shown in the column between -1 and 1°, the off-axis detectors between ± 1 and 3° and the very right off-axis detector is plotted between 3 and 5°.

Fig. 38 shows the scattering efficiency for 0.66° with the efficiency data points of the four detectors. The points are plotted in horizontal columns with a width of 2° with color-coded pixels of about. The distribution is symmetric to a central point on the x-axis in the lower quarter around θ (the resolution is also rather coarse) and therefore, similar to the Remizovich distribution shown in Fig. 4. Further pixel plots of the efficiency measurements shown in Fig. 34 and Fig. 35 can be seen in the Appendix C.2.

The on-axis scattering efficiency measurements conducted by Diebold et al. in 2015 [23], the Firsov and Remizovich model have been implemented in a GEANT4 class for grazing angle proton scattering by Guzmán et al. in 2017 [24]. The class is under development at the Institue of Astronomy and Astrophysics in Tübingen. New measurement data will also be included in the class to enable the use of recent proton scattering data.

5. Conclusions

The setup to measure grazing angle proton scattering off of X-ray mirrors has been improved. Two, respectively three off-axis detectors have been added to the setup in an array around the central detector. On- and off-axis measurements have been conducted with three SSB detectors and with in total four detectors (three PIPS together with one SSB). In preparation for these measurements, the fit routines in the detector-energy calibration with the Rutherford backscattering method have been automatized and a new, more efficient fit routine via TRIM simulations has been evaluated. The analysis framework for the scattering measurements has been adjusted to off-axis data requirements and simplified via flexible input files.
The mounting of an additional backscattering detector has been studied with simulations done in GEANT4. Results have shown that the particle flux on this detector would be too low so that there was no additional backscattering detector mounted in the experimental setup. Also, the particle detection performance of SSB and PIPS detectors has been compared in a noise study. The noise contributions to the measurements have not been stable for the PIPS and the SSB detector but depend on the data rate. Only one off-axis PIPS detector showed a constant noise behavior. The PIPS detectors also have a better signal-to-noise ratio than SSB detectors and the lower energy threshold of the PIPS detector was determined to be between 50-60 keV compared to 80-100 keV for an SSB.

The measurement results with three SSB detectors as with four detectors (PIPS and SSB) have shown, that collimator, mirror and the detector array are very well aligned and deviations from prior measurements are small. The comparison of the Remizovich model and measured data demonstrated that the maxima of the efficiencies predicted by Remizovich are higher than the measured maxima. Also, an offset between the tails of the Remizovich functions and the measured efficiencies has been, especially for the measurements at an incidence angle of 0.66° has been observed. The difference between the Remizovich model and the measured data using one on- and three off-axis detectors at an incidence angle of 0.66° is large compared to previous measurements. This could have several explanations which should be carefully checked in future studies. The incidence angle of 0.66° might be underestimated; the flux normalization via the monitor detectors could have a problem; the normalization of the analytic function needs improvement.

It may be interesting to conduct future measurements with a heat chamber to exclude scattering effects that could occur due to the humidity. To obtain ultra-high vacuum, it is necessary to heat out the vacuum chamber to get rid of residual water sticking to the surfaces. For the scattering measurements, it also has to be assumed that several atomic layers of water are adsorbed to the surface of the mirror optics. This might impact the measured scattering efficiencies. Future measurements may therefore be conducted in a heat chamber to study the possible influence.
It is also planned to conduct measurements with a silicon surface similar to the silicon pore optics that are used for *ATHENA*. And moreover, for future simulations it will be interesting to implement all recently obtained measurement results in the GEANT4 class that has been developed at the Institute of Astronomy and Astrophysics. With the past data, this effort has already been started.

A. Appendix: Experimental Setup

A.1. Data Analysis Framework: Example Input-File

Fig. 39 shows an example for an input file to map the ADC channels to the detectors in the analysis framework after it is read-in.

```
#detector type integration_low integration_high relativePosition
detDiam
#type:  0 = middle
#       1 = off-axis left
#       2 = off-axis right
#       3 = off-axis right2
#       4 = monitor 1
#       5 = monitor 2
#       6 = pulser
#Pos_rel (mm): Relative position to central detector in mm
1 4 80 8191 0 0
2 0 150 8191 0 1.25
3 1 400 8191 32 1.5
4 6 0 0 0 0
5 5 80 8191 0 0
6 2 150 8191 32 1.5
7 3 200 8191 64 2
```

Figure 39 Example for the input file of the channel-to-detector mapping with detector number, type (central, off-axis, monitor or pulser), integration limits for the spectra, relative position of the detector in milimeters and detector diameter for the size of the detector aperture.

B. Appendix - Studies and Improvements

B.1. Rutherford Plots

Fig. 40 shows the scattering distributions simulated with GEANT4 for a beam energy of 400 keV.

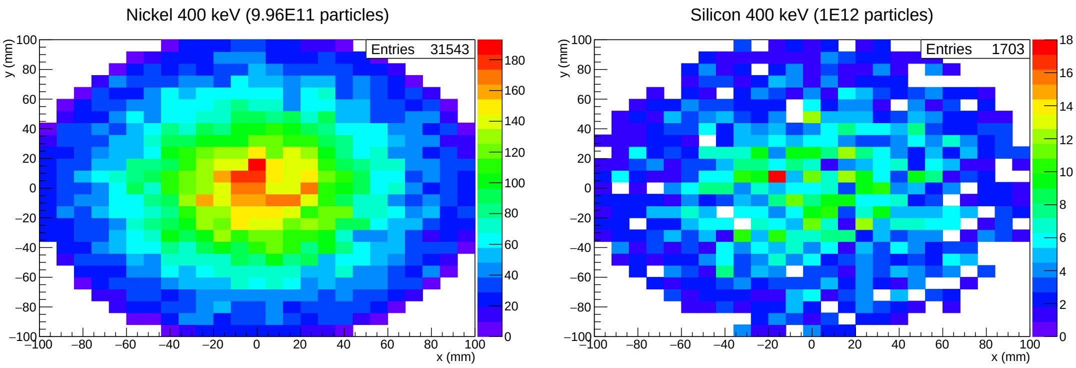

Figure 40 The two dimensional scattering distributions of simulated backscattered protons in the area of the detecting volume in the cases of nickel (left hand side) and silicon (right hand side) for a beam energy of $E_0 = 400$ keV. Each pixel corresponds to the sensitive area of a silicon surface barrier detector (with a diameter d=8 mm) used in the actual experimental setup to detect scattered particles.

B.2. Noise Plots

The noise of all analyzed runs in the noise studies are shown in Fig. 41. In Fig. 42 the residual noise for all four detectors is presented. The integral of the residual noise have been used to evaluate the noise dependent on the data rate.

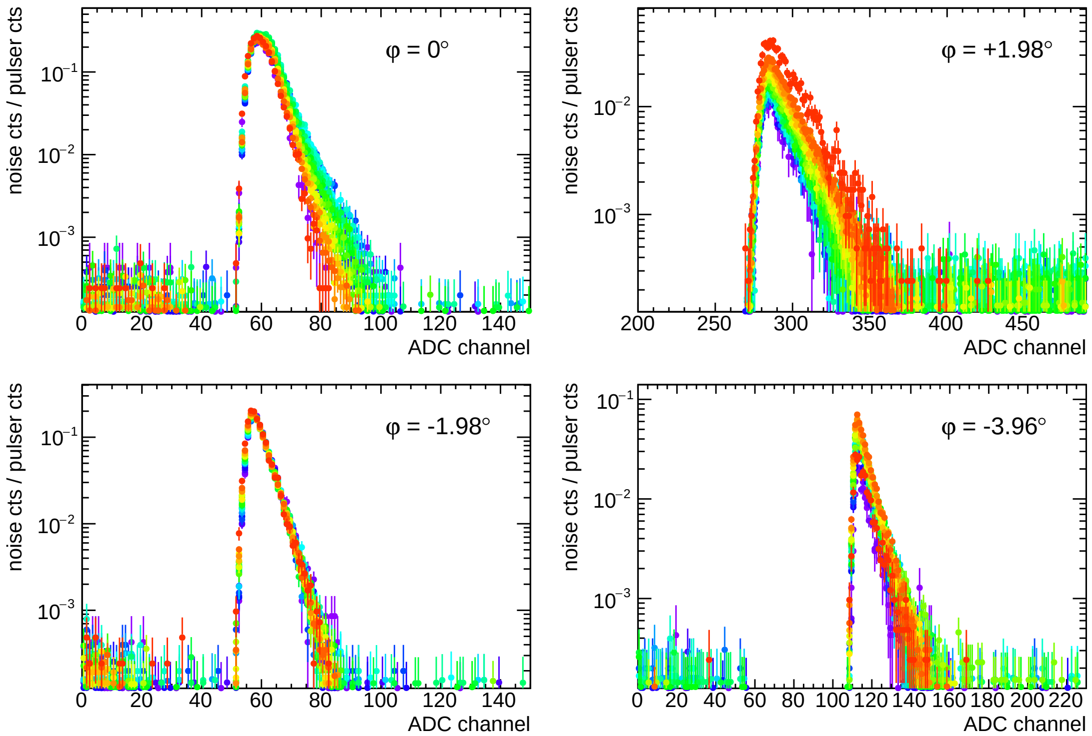

Figure 41 Noise plots for all runs and each of the four detectors: the central detector at the azimuth position $\varphi = 0°$ (top left), the off-axis detector on the left at $\varphi = +1.98°$ (top right), the off-axis detector on the right at $\varphi =$ -1.98° (bottom left) and the off-axis detector on the very right at $\varphi =$ -3.96° (bottom right). The detectors at $\varphi =$ 0, -1.98, -3.96° are PIPS detectors and the detector at $\varphi = +1.98°$ is an SSB detector.

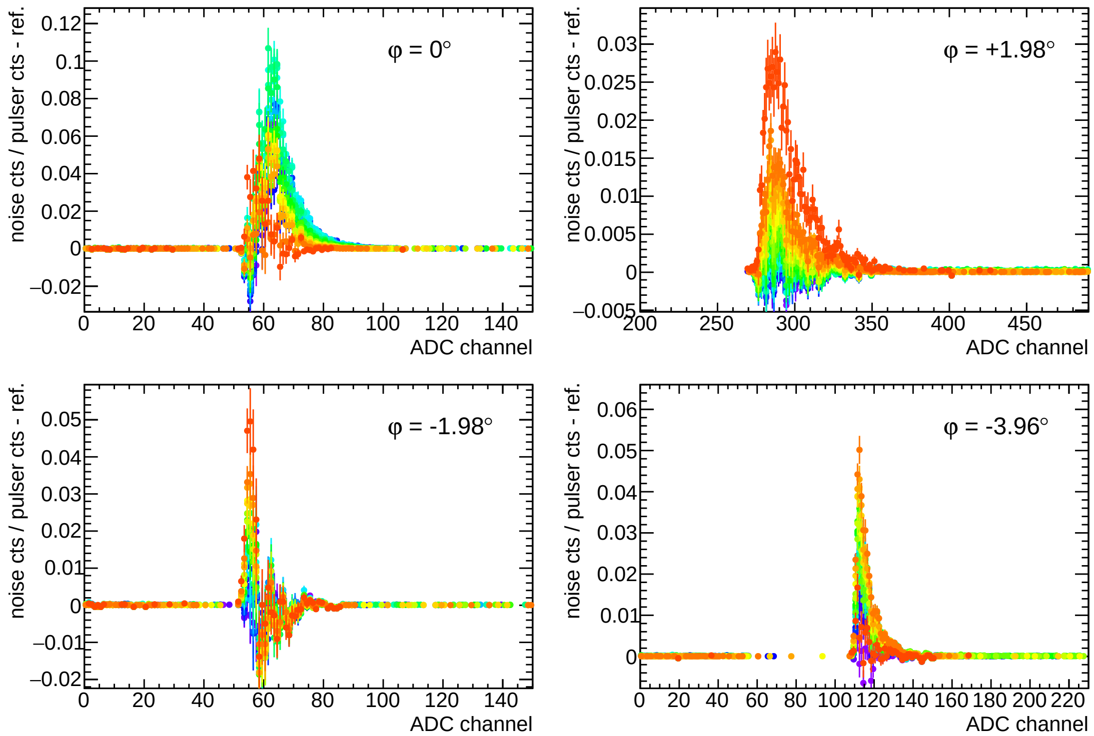

Figure 42 Residual noise for each detector. All spectra are subtracted from a reference noise run (first noise run with the accelerator turned off).

C. Appendix: Efficiency Measurement Results

C.1. TRIM Spectra

Spectra simulated with TRIM to determine the Gaussian proton spectrum after the degrader copper foil with 6 µm thickness. Mean and sigma are determined via a fit (and the FWHM calculated via the sigma of the distributions). For each primary beam energy $1{\cdot}10^5$ protons have been simulated. Furthermore, a cut has been applied to the spectra for protons with exit angle of $\pm 3°$ (so that the spectra are not averaged over all exit angles which results in a smaller mean and a larger sigma).

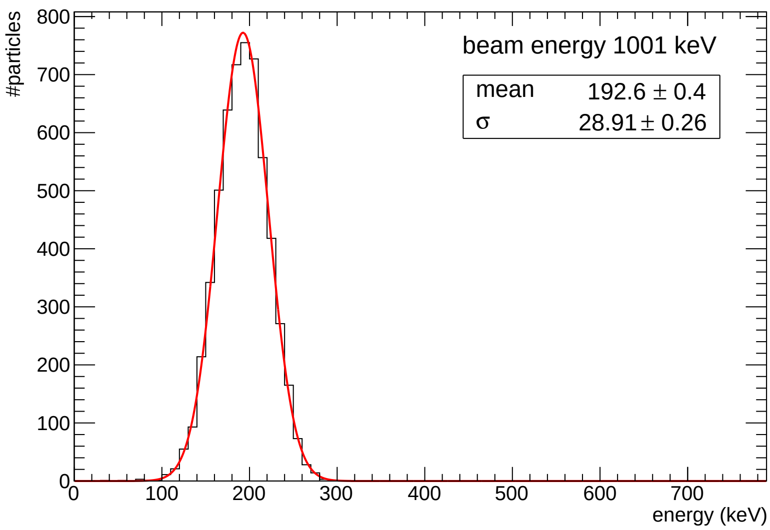

Figure 43 TRIM-simulated proton spectrum for a primary beam energy of 1001 keV and $1{\cdot}10^5$ protons. The mean value of 193 keV and FWHM of 68 keV of the spectrum after the degrader foil are determined via a Gaussian fit.

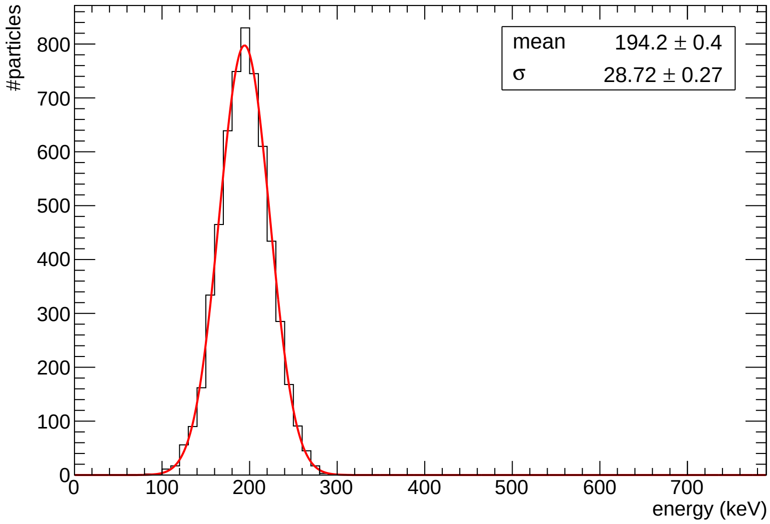

Figure 44 Same as in Fig. 43 but for a primary beam energy of 1002 keV. After the degrader foil the Gaussian proton spectrum is centered around 194 keV and has a FWHM of 68 keV.

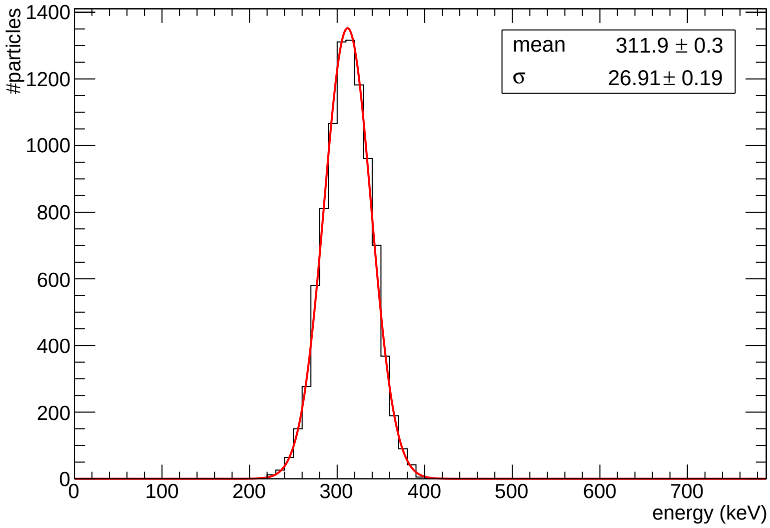

Figure 45 Same as before but for a primary beam energy of 1070 keV resulting in a Gaussian proton spectrum centered around 312 keV with a FWHM of 63 keV.

C.2. Efficiency Pixel Plots

Pixel Plots with efficiency measurements that have been presented in Fig. 34 and Fig. 35 but with data points printed in color-coded columns corresponding to the detector positions.

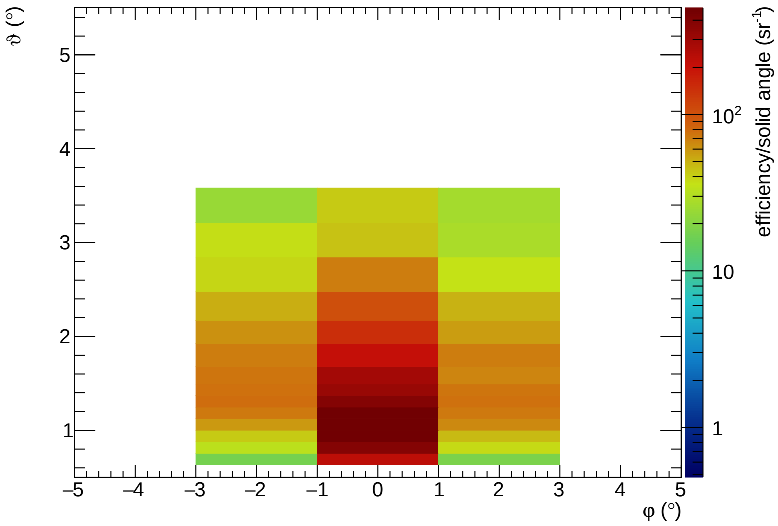

Figure 46 Efficiency measurement results for an incidence angle of 0.5° as presented in Fig. 34 in a two-dimensional plot of the scattering angle θ in relation to the azimuth angle φ. The central detector efficiency is shown in the column between -1 and 1°, the off-axis detectors between ± 1 and 3° and the very right off-axis detector is plotted between 3 and 5°.

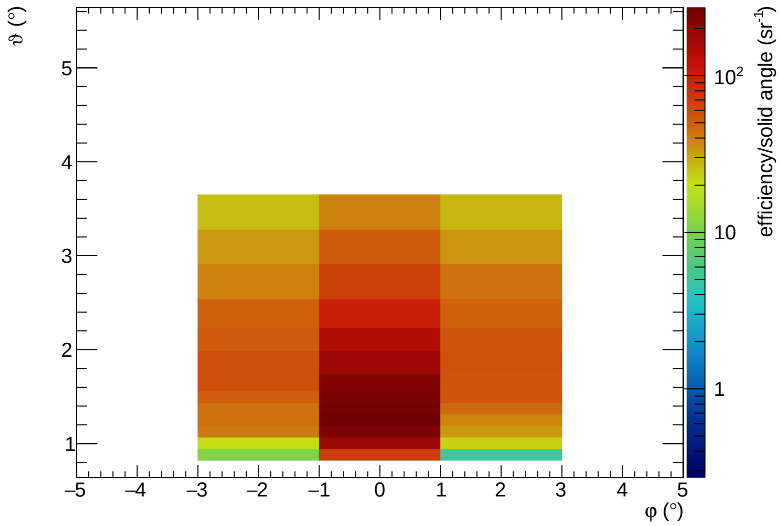

Figure 47 Same as Fig. 46, but for an incidence angle of 0.64° with corresponding efficiency measurement results presented in Fig. 34.

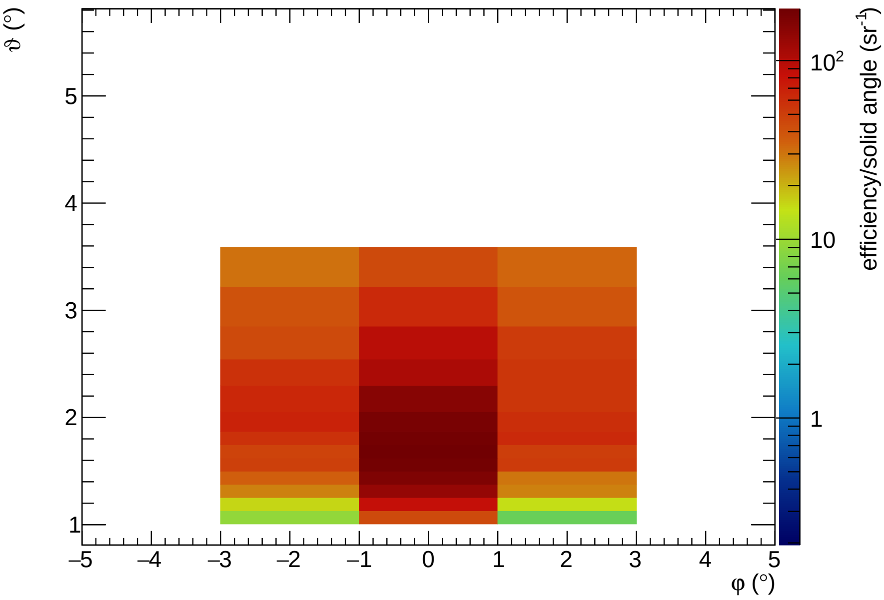

Figure 48 Same as Fig. 46, but for an incidence angle of 0.81° with corresponding efficiency measurement results presented in Fig. 35.

References

[1] F. Jansen, D. Lumb, B. Altieri, J. Clavel, M. Ehle, C. Erd, C. Gabriel, M. Guainazzi, P. Gondoin, R. Much, R. Munoz, M. Santos, N. Schartel, D. Texier, and G. Vacanti, "XMM-Newton observatory. I. The spacecraft and operations," *Astronomy & Astrophysics*, vol. 365, pp. L1–L6, 2001.

[2] E. Kendziorra, T. Clauss, N. Meidinger, M. Kirsch, M. Kuster, P. Risse, G. D. Hartner, R. Staubert, and L. Strueder, "Effect of low-energy protons on the performance of the EPIC pn-CCD detector on XMM-Newton," in *X-Ray and Gamma-Ray Instrumentation for Astronomy XI* (K. A. Flanagan and O. H. Siegmund, eds.), vol. 4140 of *Society of Photo-Optical Instrumentation Engineers (SPIE) Conference Series*, pp. 32–41, 2000.

[3] J. Carter and A. Read, "The XMM-Newton EPIC Background and the production of Background Blank Sky Event Files," *Astronomy and Astrophysics*, vol. 464, p. 1155, 2007.

[4] D. Spiga, V. Fioretti, A. Bulgarelli, E. Dell'Orto, L. Foschini, G. Malaguti, G. Pareschi, G. Tagliaferri, and A. Tiengo, "A magnetic diverter for charged particle background rejection in the SIMBOL-X telescope," *Proceedings of SPIE*, vol. 7011, no. 70112Y, 2008.

[5] J. Minow, W. Blackwell, J. Depasquale, C. Grant, S. O'dell, P. Plucinsky, D. Schwartz, B. Spitzbart, and S. Wolk, "Predicting chandra ccd degradation with the chandra radiation model," *NASA Technical Report. IAC-08-D5.3.6. ID 20090007658*, 2008.

[6] M. Weisskopf, "The Chandra X-Ray Observatory: An overview ," *Advances in Space Research*, vol. 32, no. 10, pp. 2005 – 2011, 2003.

[7] J. J. Kolodziejczak, R. F. Elsner, R. A. Austin, and S. L. O'Dell, "Ion transmission to the focal plane of the Chandra X-Ray Observatory," 2000.

[8] V. Fioretti, T. Mineo, A. Bulgarelli, P. Dondero, V. Ivanchenko, F. Lei, S. Lotti, C. Macculi, and A. Mantero, "Geant4 simulations of soft proton scattering in X-ray optics," *Experimental Astronomy*, 2017.

[9] D. Lo and J. Srour, "Modeling of proton-induced CCD degradation in the Chandra X-ray Observatory," *Nuclear Science, IEEE Transactions on*, vol. 50, no. 6, pp. 2018–2023, 2003.

[10] S. L. O'Dell, T. L. Aldcroft, B. A. Bissell, W. C. Blackwell, R. A. Cameron, J. H. Chappell, J. M. DePasquale, K. R. Gage, C. E. Grant, C. F. Harbison, M. Juda, K. A. Marsh, E. R. Martin, J. I. Minow, S. S. Murray, P. P. Plucinsky, D. A. Schwartz, D. P. Shropshire, B. J. Spitzbart, S. N. Virani, B. S. Williams, and S. J. Wolk, "Managing radiation degradation of CCDs on the Chandra X-ray Observatory II," *Proceedings of SPIE*, vol. 5898, 2005.

[11] V. Fioretti, *Background minimization issues for next generation hard X-ray focusing telescopes.* PhD thesis, University of Bologna, 2011.

[12] J. F. Ziegler, M. Ziegler, and J. Biersack, "SRIM – The stopping and range of ions in matter (2010)," *Nuclear Instruments and Methods in Physics Research Section B: Beam Interactions with Materials and Atoms*, vol. 268, no. 11–12, pp. 1818 – 1823, 2010. 19th International Conference on Ion Beam Analysis.

[13] R. Nartallo, "The propagation of low energy protons through the xmm-newton optics," *Esa/estec/tos- ema/02-067/RN Tech. Report*, 2002.

[14] B. Aschenbach, "Grazing incidence reflection and scattering of MeV protons," *Proceedings of SPIE*, vol. 6688, 2007.

[15] B. K. Dichter and S. Woolf, "Grazing angle proton scattering: effects on chandra and xmm-newton x-ray telescopes," *Nuclear Science, IEEE Transactions on*, vol. 50, no. 6, pp. 2292–2295, 2003.

[16] F. Lei, R. Nartallo, P. Nieminen, E. Daly, H. Evans, and P. Truscott, "Update on the Use of Geant4 for the Simulation of Low-Energy Protons Scattering Off X-Ray Mirrors at Grazing Incidence Angles," *IEEE Transactions on Nuclear Science*, vol. 51, pp. 3408–3412, 2004.

[17] H. Winter, M. Wilke, and M. Bergomaz, "Energy loss of fast protons in grazing scattering from an al(111)-surface," *Nuclear Instruments and Methods in Physics Research Section B: Beam Interactions with Materials and Atoms*, vol. 125, no. 1, pp. 124 – 127, 1997.

[18] R. Pfandzelter and F. Stölzle, "Probing the stopping power near the surface by specular reflection of protons from graphite," *Nuclear Instruments and Methods in Physics Research Section B: Beam Interactions with Materials and Atoms*, vol. 72, no. 2, pp. 163 – 175, 1992.

[19] Y.-H. Song and Y.-N. Wang, "Numerical simulation for H+ ion-surface scattering under grazing incidence," *Nuclear Instruments and Methods in Physics Research Section B: Beam Interactions with Materials and Atoms*, vol. 153, no. 1, pp. 186 – 190, 1999.

[20] O. B. Firsov, "Reflection of Fast Ions from a Dense Medium at Glancing Angles," *Soviet Physics Doklady*, vol. 11, pp. 732–733, 1967.

[21] V. Remizovich, M. Ryazanov, and I. Tilinin, "Energy and angular distributions of particles reflected in glancing incidence of a beam of ions on the surface of a material," *Zhurnal Eksperimentalnoi i Theoreticheskoi Fiziki*, vol. 79, pp. 448–458, 1980.

[22] N. Kuwata, K. Kimura, and M.-H. Mannami, "Small angle scattering of mev protons at glancing incidence on au and ag targets," *Nuclear Instruments and Methods in Physics Research Section B: Beam Interactions with Materials and Atoms*, vol. 1, no. 1, pp. 35 – 40, 1984.

[23] S. Diebold, C. Tenzer, E. Perinati, A. Santangelo, M. Freyberg, P. Friedrich, and J. Jochum, "Soft proton scattering efficiency measurements on x-ray mirror shells," *Experimental Astronomy*, vol. 39, pp. 343–365, Jun 2015.

[24] A. Guzmán, E. Perinati, S. Diebold, C. Tenzer, and A. Santangelo, "A revision of soft proton scattering at grazing incidence and its implementation in the geant4 toolkit," *Experimental Astronomy*, pp. 1–11, 2017.

[25] Website of the National Institue of Standars and Technology (NIST), "Calculation of the stopping power and range tables for protons (PSTAR), for helium ions (ASTAR) and electrons (ESTAR) for various materials." https://physics.nist.gov/PhysRefData/Star/Text/appendix.html. (Accessed December 13, 2017).

[26] S. Diebold, P. Azzarello, E. D. Monte, M. Feroci, J. Jochum, E. Kendziorra, E. Perinati, A. Rachevski, A. Santangelo, C. Tenzer, A. Vacchi, G. Zampa, and N. Zampa, "A setup for soft proton irradiation of x-ray detectors for future astronomical space missions," *Nuclear Instruments and Methods in Physics Research Section A: Accelerators, Spectrometers, Detectors and Associated Equipment*, vol. 721, no. Supplement C, pp. 65 – 72, 2013.

[27] R. Brown and D. Powers, "Precision ion beam energy measurement of a Van de Graaff accelerator using a generating voltmeter," vol. 151, pp. 377–380, 1978.

[28] P. Kump, V. Ramšak, P. Rupnik, and M. Vakselj, "An absolute calibration of electrostatic accelerators in the energy region from 0.7 MeV to 2.1 MeV," *Nuclear Instruments and Methods*, vol. 112, pp. 489–494, 1973.

[29] S. Diebold, S. Hanschke, E. Perinati, R. Smith, C. Tenzer, A. Santangelo, and J. Jochum, "Updates on experimental grazing angle soft proton scattering," *Proceedings of SPIE*, vol. 10397, 2017.

[30] Predehl, Peter et al., "eROSITA on SRG," *Proceedings of SPIE*, vol. 9144, 2014.

[31] C. Leroy and P.-G. Rancoita, *Principles Of Radiation Interaction In Matter And Detection*, vol. 3. 2012.

[32] Homepage of the Centre National des Sciences et Technologies Nucleaires, "Solid state detectors." http://www.cnstn.rnrt.tn/afra-ict/NAT/alpha/html/solidetecto.htm. (Accessed November 25, 2017).

[33] J. R. Batten, "Evaluation of passivated ion implanted planar silicon detectors for the spectroscopy and assay of low energy electrons," *Nuclear Instruments and Methods in Physics Research Section A: Accelerators, Spectrometers, Detectors and Associated Equipment*, vol. 277, no. 2, pp. 478 – 484, 1989.

[34] G. F. Knoll, *Radiation detection and measurement.* New York, NY; Weinheim u.a: Wiley, 3 ed., 2000.

[35] M. Oetliker, "Response of a passivated implanted planar silicon (PIPS) detector for heavy ions with energies between 25 and 360 keV," *Nuclear Instruments and Methods in Physics Research Section A: Accelerators, Spectrometers, Detectors and Associated Equipment*, vol. 337, no. 1, pp. 145 – 148, 1993.

[36] "PIPS Detectors. Passivated Implanted Planar Silicon Detectors.." http://www.canberra.com/products/detectors/pdf/passivated_pips_C39313a.pdf. (Accessed December 16, 2017).

[37] S. Agostinelli, et al., "GEANT4: A Simulation toolkit," *Nuclear Instruments & Methods in Physics Research, Section A: Accelerators, Spectrometers, Detectors, and Associated Equipment*, vol. 506, pp. 250–303, 2003.

[38] M. Bavdaz, E. Wille, M. Ayre, I. Ferreira, B. Shortt, S. Fransen, M. Collon, G. Vacanti, N. Barriere, B. Landgraf, J. Haneveld, C. van Baren, K.-H. Zuknik, D. D. M. Ferreira, S. Massahi, F. Christensen, M. Krumrey, V. Burwitz, G. Pareschi, D. Spiga, G. Valsecchi, D. Vernani, P. Oliver, and A. Seidel, "The ATHENA telescope and optics status," 2017.

[39] M. Mayer, "SIMNRA User's Guide 6.05," *Max-Planck-Institut für Plasmaphysik, Garching*, 2009.

[40] R. Salomonovič, "Angular distribution of proton non-rutherford elastic scattering cross section of carbon and silicon," *Nuclear Instruments and Methods in Physics Research Section B: Beam Interactions with Materials and Atoms*, vol. 82, no. 1, pp. 1 – 6, 1993.

[41] Ž. Šmit, "Rutherford backscattering from a thick target," *Physical Review A*, vol. 48, pp. 2070–2076, 1993.